

## Validation and intercomparison of three mesoscale models on three FASTEX cloud systems: Comparison with coarse-resolution simulations

By PHILIPPE LOPEZ<sup>1\*</sup>, KLARA FINKELE<sup>2</sup>, PETER CLARK<sup>3</sup> and PATRICK MASCART<sup>4</sup>

<sup>1</sup>*Météo-France, Centre National de Recherches Météorologiques, Toulouse, France*

<sup>2</sup>*Met Éireann, Dublin, Ireland*

<sup>3</sup>*Met Office, Joint Centre for Mesoscale Meteorology, Reading, UK*

<sup>4</sup>*Centre National de la Recherche Scientifique, Laboratoire d'Aérodynamique, Toulouse, France*

(Received 21 June 2001; revised 20 December 2002)

### SUMMARY

Taking advantage of the observations collected during the Fronts and Atlantic Storm-Track EXperiment (FASTEX), three FASTEX midlatitude cloud systems are simulated with three state-of-the-art, mesoscale, limited-area models (the Met Office's Unified Model (UM), Met Éireann's High Resolution Limited Area Model (HIRLAM), and the French Laboratoire d'Aérodynamique recherche modèle de Mésos-échelle Non-Hydrostatique (Mésos-NH)), at an 11 km horizontal resolution and with about 50 vertical levels. The dynamical, thermodynamic, cloud and precipitation fields obtained from these numerical integrations are then intercompared and validated against various observational sources, including radio- and dropsondes, satellite radiometer, and rain-gauges. The similarities and the deficiencies of the three models are summarized in the paper. After this validation work, the mesoscale fields are degraded in resolution, so that they can be directly compared with the outputs of 300 km resolution simulations, run with Météo-France's atmospheric general-circulation model (AGCM) Action de Recherche Petite Echelle et Grande Echelle (ARPEGE). The deviations between the upscaled mesoscale models and the coarse AGCM turn out to be significant and highly dependent on the location relative to the storm, with, in particular, a large contrast between the trailing cold region and the warm sector with thick layer clouds, suggesting the existence of some deficiencies in the AGCM.

KEYWORDS: FASTEX Mesoscale simulations Upscaling

### 1. INTRODUCTION

In recent years, the correct representation of cloud-related processes and their various effects on the environment has proven to figure among the key issues for properly simulating the Earth's climate by means of atmospheric general-circulation models (AGCMs). The interaction of cloud systems with the rest of the atmosphere is mainly active through condensational heating, radiation, and precipitation. Besides, previous studies have also suggested that the current coarse-resolution AGCMs should include some parametrizations of the bulk effects of subgrid-scale circulations, such as the ones encountered in the frontal zones of midlatitude synoptic cyclones (e.g. Szeto and Guan 2000). Note that throughout this paper the term 'resolution' will stand for the 'grid spacing' of a given model. One approach to isolating the deficiencies of AGCMs consists of comparing coarse-resolution AGCM simulations of some selected meteorological event with some high-resolution simulations of the same event, averaged over the AGCM resolution, and obtained from one or several limited-area models (LAMs). Of course, in such a method it is essential, as a first step, to intercompare and to validate the simulations obtained from the high-resolution models. This strategy was applied by Ryan *et al.* (2000) to the case of an Australian extratropical cloud system, the high-resolution runs being provided by a set of cloud-resolving and limited-area models, with 5 and 20 km horizontal resolutions, respectively. An intercomparison of regional mesoscale models at various resolutions in the case of an explosive oceanic cyclogenesis, was also performed by Gyakum *et al.* (1996), who showed that the main improvement on the simulated mass, wind, and precipitation fields was obtained when

\* Corresponding author, present address: ECMWF, Shinfield Park, Reading, Berkshire RG2 9AX, UK.  
e-mail: p.lopez@ecmwf.int

© Royal Meteorological Society, 2003. Peter Clark's contribution is Crown copyright.

the horizontal resolution was enhanced from 100 km to 50 km. They also indicated that a further increase of the resolution did not lead to a substantial improvement of the forecasts. However, going down to a 10 km resolution should benefit from the more explicit representation of small-scale phenomena.

As part of the FASTEX\* Cloud System Study (FASTEX-CSS) European project, the final aim of our study was to compare simulations of extratropical winter cloud systems which were obtained with a coarse-resolution (300 km) AGCM, on the one hand, with high-resolution (11 km) simulations obtained with three mesoscale LAMs, on the other hand. Prior to the final upscaling procedure which was applied to the mesoscale simulations, they were intercompared and validated against the observations collected in January and February 1997 over the North Atlantic, during FASTEX.

Section 2 is devoted to the general set-up of the experiments, including a description of the three studied cloud systems, an overview of the models, and a summary of the data that were used in the validation procedure. In section 3, first, the forecast standard dynamical and thermodynamic fields are intercompared and validated against sonde observations. Secondly, a similar account focuses on clouds and precipitation, which includes a validation against Meteosat data and rain-gauge measurements. This section ends with the presentation of global heat budgets computed from the high-resolution runs. Section 4 compares 300 km resolution fields from the Action de Recherche Petite Echelle et Grande Echelle (ARPEGE) AGCM with the corresponding fields from the mesoscale models, after their averaging at the AGCM coarse resolution. An attempt to relate the resulting deviations to the location relative to the storm is then presented. Section 5 outlines the conclusions of the paper.

## 2. PRESENTATION

### (a) *The studied cases*

The three cases which were simulated with the mesoscale models, were selected from among the 19 Intensive Observing Periods (IOPs) of midlatitude cloud systems during the FASTEX field campaign in January and February 1997 over the North Atlantic (see Joly *et al.* 1999). An atlas of meteorological maps and satellite pictures describing the two months of FASTEX can be found at the FASTEX website (<http://www.cnrm.meteo.fr/dbfastex/>, November 2002). IOPs 11, 16 and 17 were chosen because they correspond to winter cloud systems associated with intense lows, and include excellent observational coverage by the fleet of FASTEX aircraft.

The IOP 11 case was a cyclone that formed over the east of North America on 3 February 1997, then intensified while crossing the Atlantic, and finally passed north of the British Isles on 6 February 1997. This cyclone shows two features that were highlighted by the FASTEX project: on one hand, a 'complex life cycle', meaning that the cyclone underwent several distinct phases of development, and on the other hand, cyclogenesis by splitting. IOP 11 is the best illustrated example in the overview of the FASTEX cases proposed by Baehr *et al.* (1999).

IOP 16 started as a wave that rapidly deepened beneath the moving end of a jet streak, from 0000 UTC 17 February 1997, in the middle of the North Atlantic, until 0600 UTC 18 February 1997, east of Iceland. Most of its life cycle took place in the eastern half of the North Atlantic storm track, within reach of the FASTEX turboprop aircraft that captured the early stage of its development. In particular, its associated

\* Fronts and Atlantic Storm-Track EXperiment.

cloud system passed over the British Isles on 17 February 1997, and its well developed cloud head and dry intrusion were sampled in detail by the FASTEX aircraft.

IOP 17, which has often been referred to as the ‘FASTEX cyclone’, was a well sampled cyclone, characterized by a complex life cycle. It was initiated mainly through the barotropic influence of a pre-existing surface low located close to the Great Lakes on a baroclinic zone over the western North Atlantic (Arbogast and Joly 1998). The first explosive deepening ( $-35 \text{ hPa day}^{-1}$ ) was observed at 1800 UTC 17 February 1997. The second phase of intensification occurred at 1200 UTC 18 February 1997. Mallet *et al.* (1999) showed that, during this phase, diabatic processes took over the baroclinic development, leading to a decoupling of the altitude and surface disturbances, and a splitting of the upper-tropospheric jet streak. The strongest deepening ( $-64 \text{ hPa day}^{-1}$ ) was observed at 1200 UTC 19 February 1997, while crossing the jet, and the minimum surface pressure (941 hPa) was reached at 0000 UTC 20 February 1997, over the Norwegian Sea. More details on the life cycle of IOP 17 can be found in Cammas *et al.* (1999) and Mallet *et al.* (1999).

It should be noted that for the sake of brevity, field maps will be shown for IOPs 11 and 16 only, while more synthetic statistical results will be presented for all three cases.

### (b) *The mesoscale models*

Three FASTEX research groups agreed to run their own mesoscale limited-area models for simulating the two selected cases: the Met Office with the Unified Model (UM, hereafter), Met Éireann with the High Resolution Limited Area Model (HIRLAM), and the Laboratoire d’Aérodynamique with the French research modèle de Mésoscale Non-Hydrostatique (Mésos-NH). Table 1 summarizes the main parametrizations and technical characteristics of the three mesoscale models; Météo-France’s global model ARPEGE which will be referred to in section 4, has also been included in the table. Any further details on each model can be found in the bibliographical references cited in Table 1.

### (c) *Set-up of the simulations*

In order to get a good compromise between computational cost and the fulfilment of technical constraints inherent in limited-area modelling, the size of the integration domain, the target resolution and the duration of the mesoscale simulations were set to  $1500 \text{ km} \times 1500 \text{ km}$ , approximately 11 km, and 12 hours, respectively. Such configuration ensured that, for each of the three FASTEX cases, the cloud system of interest was located within the LAM domain throughout the 12-hour integration. It should be noted that some earlier simulations obtained from the UM on FASTEX cases indicated that increasing the forecast length up to 18 hours and enlarging the integration domain with a coarser resolution (24 km) did not lead to qualitatively different forecasts, especially in terms of the large-scale structure of the cloud fields. This suggested that longer simulations would not significantly change the structure of the forecast errors. The results of these experiments as well as the desire to obtain a useful three-dimensional (3D) maximum-resolution database for the selected extratropical cloud systems dictated our final choice for the resolution and the forecast length mentioned above.

Since, as part of the FASTEX project, re-analyses of the two months of the field campaign were obtained from the four-dimensional variational (4D-Var) assimilation system that recently became operational in Météo-France’s global ARPEGE model (Desroziers *et al.* 1999) these data were used as initial and boundary conditions in the three LAMs. This ARPEGE 4D-Var re-analysis dataset has the great advantage

TABLE 1. CHARACTERISTICS OF THE MODELS USED IN THIS STUDY

Model feature	UM	HIRLAM	Méso-NH	ARPEGE
Model domain	Limited	Limited	Limited	Global
Field representation	Grid point	Grid point	Grid point	Spectral
Vertical coordinate	$\sigma - P$	$\sigma - P$	$z$ (Gal-Chen and Somerville 1975)	$\sigma - P$
Horizontal grid	Lat.-long.	Lat.-long.	Polar stereographic	Stretched reduced Gaussian
Formulation	Hydrostatic	Hydrostatic	'Pseudo-incompressible'	Hydrostatic
Number of vertical levels	47	45	Non-hydrostatic (Durran 1989)	31
Horizontal resolution (dx,dy)	0.17/0.10 deg	0.17/0.10 deg	$\approx 11$ km	T42 ( $\approx 300$ km)
Prognostic microphysical variables	$q_v, q_i, (q_i + q_s)$	$q_v, (q_i + q_i)$	$q_v, q_i, q_i, q_r, q_s, q_g$	$q_v, (q_i + q_i), (q_r + q_s)$
Type of nesting	1-way (2 steps)	1-way (2 steps)	2-way (1 step) (Stein <i>et al.</i> 2000)	/
Relaxation at boundary	Davies (1976)	Davies (1976)	Chen (1991); Carpenter(1982)	/
Advection scheme	Eulerian	Semi-Lagrangian	Eulerian	Semi-Lagrangian
Convection scheme	Gregory and Rowntree (1991)	Kain and Fritsch (1990)	Bechtold <i>et al.</i> (2000)	Bougeault (1985)
	Bulk cloud, mass flux	Bulk cloud, mass flux	Kain-Fritsch type, mass flux	Bulk cloud, mass flux
Large-scale condensation and microphysics	Smith (1990)	Rasch and Kristjánsson (1998)	Stein <i>et al.</i> (2000)	Smith (1990)
	Wilson and Ballard (1999)		Pinty and Jabouille (1998)	Lopez (2002)
Radiation	Slingo and Wilderspin (1986)	Savijärvi (1990)	Fouquart and Morcrette (Morcrette 1990)	Geleyn <i>et al.</i> (1995)
	Slingo (1985), Slingo (1989)			
Turbulence		Holtslag and Boville (1993)	Bougeault and Lacarrère (1989)	Louis (1979), Geleyn (1987)
Horizontal diffusion	4th order	4th order	4th order	6th order
General description	Cullen (1993)	Källén (1996)	Bougeault <i>et al.</i> (1999)	Courtier <i>et al.</i> (1991)

UM is the Met Office Unified Model, Méso-NH is the French Laboratoire d'Aéologie research modèle de Méso-échelle Non-Hydrostatique, and HIRLAM is Met Éireann's High Resolution Limited Area Model.  $q_v$  = water-vapour specific content,  $q_i$  = cloud liquid-water content,  $q_l$  = cloud ice content,  $q_r$  = rain content, and  $q_g$  = graupel content.

of including most of the non-conventional observations which were deployed during FASTEX over the North Atlantic, such as dropsoundings, enhanced radiosoundings from land stations and FASTEX ships, as well as buoy measurements. The re-analysis datasets provided to the mesoscale modellers had a horizontal resolution of about 50 km over the North Atlantic area, which is consistent with the finest length-scales resolvable with Météo-France's current 4D-Var assimilation procedure. The basic re-analysed fields were temperature, wind, and specific humidity, available on the standard ARPEGE 31  $\sigma$ - $P$  vertical levels, as well as surface pressure and surface temperature.

Given that early 11 km LAM simulations which were directly initialized from the 50 km resolution re-analysis data, led to unsatisfactory results due to the effects of boundary relaxation on the propagation of the simulated cloud system, the choice was made to apply a nesting method. Therefore, for both UM and HIRLAM, starting from the re-analysis, an intermediate run (approximately 22 km resolution) was first performed over a larger domain that encompassed most of the North Atlantic. In turn, the 22 km outputs could then be used as initial and boundary conditions for completing the expected 11 km simulations. For Mésó-NH, a slightly different, single-step, two-way nesting technique is used (Stein *et al.* 2000). In this approach, the intermediate-resolution (22 km) and the high-resolution (11 km) models are run simultaneously to allow a two-way interaction. The intermediate-resolution model is driven by the 3-hourly ARPEGE re-analysis, whereas the high-resolution model receives its boundary conditions directly from the coarser model at every time step. A permanent interaction between the two models is thereby obtained in a single step.

#### (d) Validation data

The observational datasets which were looked at in the present study are listed below. For each data type, an abbreviated name and the practical horizontal resolution of the dataset is mentioned:

- Meteosat brightness temperatures (BT) in the infrared (IR, 7.5 km) and water vapour (WV, 5 km) channels. Thanks to the radiative-transfer model originally developed by Morcrette (1991), it was possible to compute simulated BTs in the Meteosat IR- and WV-frequency windows from the model fields, after some slight adaptation to the grid geometry used in this intercomparison. It must be noted that such retrievals include the radiative effect of the forecast cloud condensate (Roca *et al.* 2000). Chaboureau *et al.* (2000) gives an example of the application of Morcrette's radiative model to a FASTEX case.
- Measurements of temperature, wind, and relative humidity, provided by the radiosounding conventional network.
- Similar data obtained from the dropsondes that were released from the UK C-130 and National Oceanic and Atmospheric Administration (NOAA) Gulfstream IV aircraft during FASTEX IOPs.
- Surface precipitation measurements from the UK and Irish conventional observing networks.
- Radar data from the X-band radar installed on board the NOAA P3 aircraft.
- Airborne *in situ* two-dimensional cloud (2D-C) probe measurements of cloud water: since the work by Forbes *et al.* (2000) demonstrated that trying to validate the simulated cloud condensate against such observations was rather inconclusive, no further attempt was carried out here.

It should be noted that some radiosonde and dropsonde data were assimilated inside the  $\pm 3$ -hour assimilation window of the ARPEGE 4D-Var analysis in order to provide

the initial conditions for the mesoscale runs. To avoid any problem of dependence, only later sonde data were used in the validation of the mesoscale forecasts.

### 3. MESOSCALE MODEL RESULTS

#### (a) *Standard meteorological fields*

(i) *Model intercomparison.* The first intercomparison to be presented here, will focus on the ability of the three mesoscale models to simulate the standard dynamical and thermodynamic fields that describe the large-scale features of the flow.

To give a first overview of each simulation, Fig. 1 shows the 12-hour forecast mean-sea-level pressure (MSLP) and 850 hPa relative vorticity for the three models, and for IOPs 11 and 16. Figure 2 displays the 12-hour forecast of 300 hPa wind speed, superimposed onto the 850 hPa equivalent potential-temperature field ( $\theta_e$ ).

In the simulations of IOP 11, Figs. 1(a)–(c) point out patterns in the 850 hPa vorticity and MSLP fields that are consistent among models. In particular, the low is only slightly deeper when simulated by either Méso-NH or HIRLAM (978 hPa), than with UM (981 hPa). The three models simulate the same three main bands of positive vorticity, but the maximum values of this field are much larger in HIRLAM than in Méso-NH, and higher in Méso-NH than in UM. The first vorticity band (B1) which stretches from the south-west of the domain to the centre of the low, is associated with the cold front, labelled (CF) in Fig. 2(a). The second stripe (B2) which runs from the centre of the low up to the north-eastern corner of the domain, corresponds to the remnants of a former cold front. A third band (B3) that bends eastwards away from the MSLP minimum, is associated with the warm front, labelled (WF) in Fig. 2(a). The vorticity field exhibits a higher spatial variability in Méso-NH than in HIRLAM, and in HIRLAM than in UM. This is related to the use of different coefficients in the numerical diffusion scheme, but also to the non-hydrostatic formulation of Méso-NH. Figures 2(a)–(c) also show that the maximum 300 hPa wind speed is higher in Méso-NH ( $80 \text{ m s}^{-1}$ ) than in UM ( $75 \text{ m s}^{-1}$ ) and HIRLAM ( $71 \text{ m s}^{-1}$ ). Furthermore, it is noteworthy that a break appears in the middle of the jet streak simulated by all models (label JB in Fig. 2(a)), which separates a secondary maximum of wind speed in the south-west, from the main maximum located further north (around  $58^\circ\text{N}$ ). This flow pattern at 300 hPa could not be detected in the 4D-Var FASTEX re-analysis (not shown), but previous studies have demonstrated that such a double structure of the jet originates from an enhancement of the ascent by diabatic processes (e.g. Mallet *et al.* 1999). The northernmost jet streak can be seen as an outflow jet, labelled OJ in Fig. 2(a), that caps the slantwise ascent above the core of the developing low (Cammass *et al.* 1999). The calculation of the non-divergent wind component at 300 hPa (not shown) revealed the existence of a clear minimum value at the location of the jet break. This suggests that the double jet structure is primarily related to the strengthening of the gradient of potential vorticity at the tropopause downshear from the heating, and not directly to the divergence. The fact that the double jet structure is present in the mesoscale runs, but not in the re-analysis, could very well be the consequence of the enhanced horizontal and vertical resolutions used in the LAM simulations.

For IOP 16, Figs. 1(d)–(f) reveal the presence of three simulated main bands of significant positive relative vorticity at 850 hPa, in all three models. The first band (B1), which coincides with the simulated cloud head (label CH in Fig. 2(d)), as illustrated further down, has its maximum in the vicinity of the MSLP local minimum at point ( $57^\circ\text{N}$ ,  $15^\circ\text{W}$ ). This local minimum is slightly lower with Méso-NH (961 hPa) than

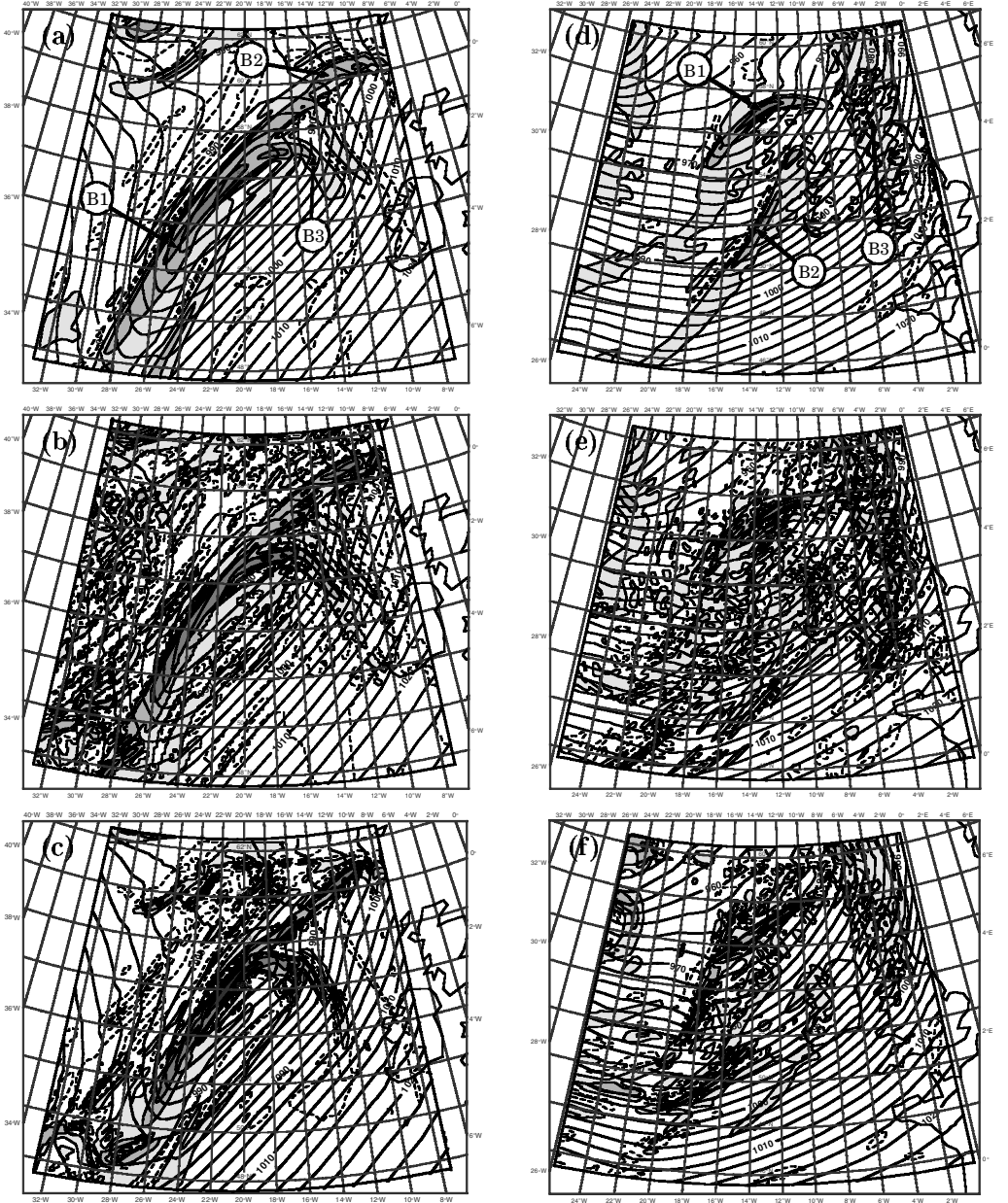


Figure 1. 12-hour forecast 850 hPa relative-vorticity and mean-sea-level pressure (MSLP) fields for FASTEX IOP 11 (left column) and IOP 16 (right column), from UM ((a) and (d)), Méso-NH ((b) and (e)), and HIRLAM ((c) and (f)). Contour interval for MSLP is 2.5 hPa, while for relative vorticity, the plotted isolines correspond to  $-50, -30, -10, -5, 5, 10, 30, 50, 100$  and  $200 (\times 10^{-5} \text{ s}^{-1})$ . Darker and darker grey shading shows regions where vorticity increases from  $5 \times 10^{-5} \text{ s}^{-1}$ . Labels B1, B2, and B3 point to the vorticity bands described in the text. See text for explanation of acronyms.

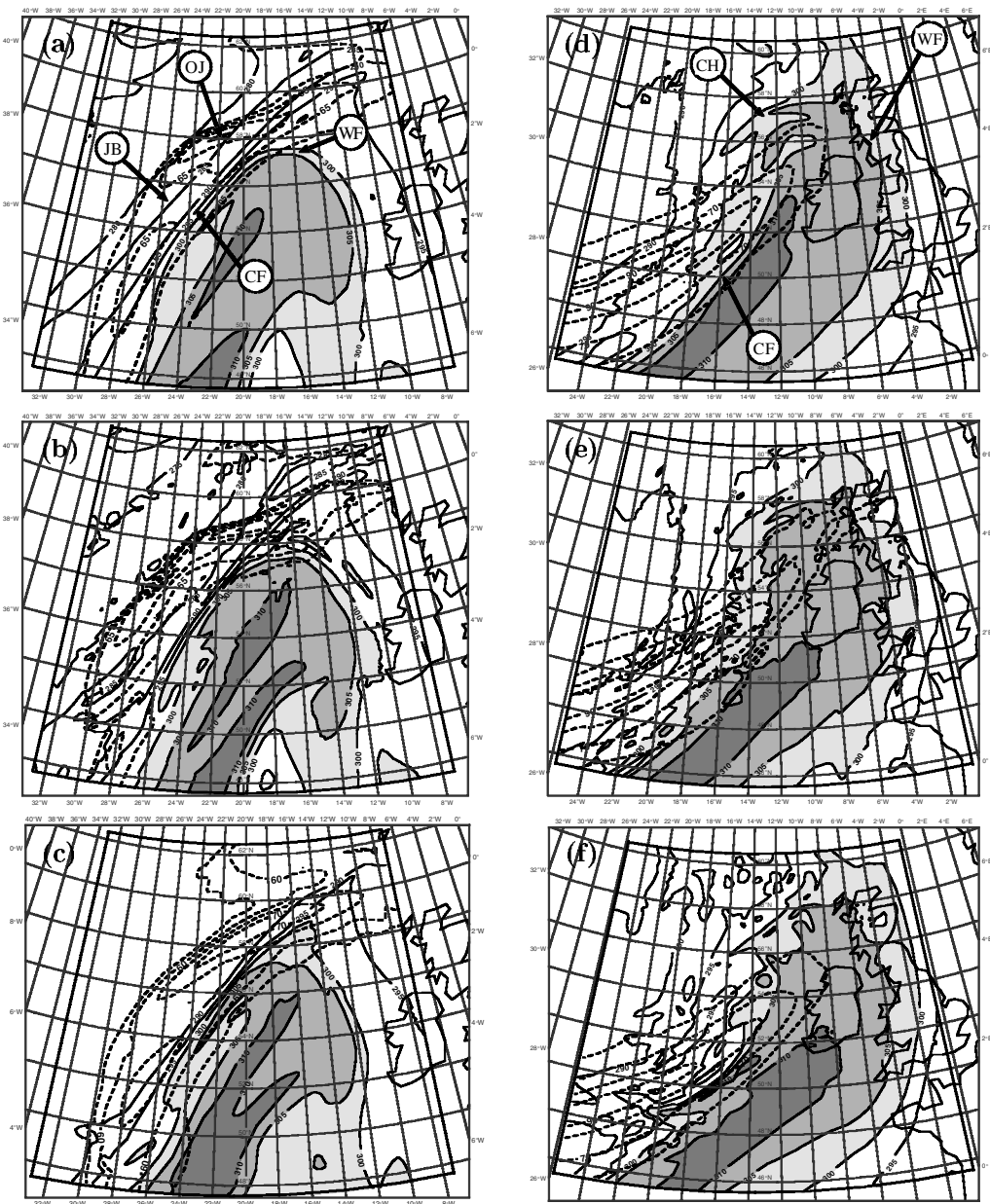


Figure 2. Same as Fig. 1 but for 12-hour forecast 850 hPa equivalent potential temperature ( $\theta_e$ ) and 300 hPa wind speed. Only values of wind speed exceeding  $60 \text{ m s}^{-1}$  are shown, with an interval of  $5 \text{ m s}^{-1}$  for IOP 11 and  $10 \text{ m s}^{-1}$  for IOP 16. Isotherms are drawn every 5 K, with a grey shading for values above 300 K. Labels CF, WF, JB, OJ, and CH, respectively, stand for cold front, warm front, jet break, outflow jet, and cloud head, mentioned in the text.



with UM and HIRLAM (963 hPa). A second band (B2) is clearly associated with the cold front (label CF in Fig. 2(d)), which looks sharper in UM and HIRLAM than in Méso-NH. However, this band exhibits a more zonal orientation in HIRLAM than in the two other models, in relation to a corresponding orientation of the isolines of equivalent potential temperature (Fig. 2(f)). A less organized and weaker third band (B3) associated with the warm front ahead of the system (label WF in Fig. 2(d)) affects Scotland and the north of Wales. Lastly, the simulated 300 hPa jet streak has a substantially stronger core in Méso-NH ( $100 \text{ m s}^{-1}$ ), than in UM and HIRLAM ( $94 \text{ m s}^{-1}$ ), but the structure of the jet streak is very similar in all models.

In order to obtain a more general insight into the variability among the three models, Fig. 3 displays vertical profiles of the mean and root mean square (r.m.s.) differences between each pair of models for temperature, specific humidity and wind, for IOP 11, at 0000 UTC 6 February 1997. Figure 4 shows the same statistics for IOP 16, at 1200 UTC 17 February 1997. It should be underlined that such an intercomparison does not allow the actual skill of each model to be judged. The two cases selected for plotting very clearly exhibit some common features. As for temperature, the average absolute deviations remain smaller than 1 K throughout the troposphere. In both cases UM is slightly warmer than Méso-NH inside the planetary boundary layer (PBL), but colder by up to 0.5 K in all layers between 850 hPa and the tropopause. At the same time, HIRLAM is substantially warmer than the two other models by up to 1 K between 600 hPa and the surface. HIRLAM is also significantly colder than Méso-NH between 600 hPa and the tropopause. In terms of specific humidity, HIRLAM is clearly much drier than the two other models in the lowest part of the troposphere, while UM and Méso-NH do not differ by more than  $0.1 \text{ g kg}^{-1}$ , even close to the surface. For the wind speed, Fig. 3(c) and Fig. 4(c) indicate that Méso-NH produces stronger winds than UM and HIRLAM, especially inside the PBL. This difference will be demonstrated, by comparison with observed soundings, to be largely an overestimation by Méso-NH.

For two given models, the r.m.s. difference includes contributions from both their mean difference and their spatial covariance. For temperature, the r.m.s. differences range between 0.6 and 1.4 K for both cases examined in Fig. 3(d) and Fig. 4(d). As regards specific humidity, the r.m.s. differences follow the natural decrease of this field with height, with values reaching  $0.5 \text{ g kg}^{-1}$  close to the surface. In the IOP 16 case, the large differences between HIRLAM and the two other models inside the PBL clearly enhance the corresponding r.m.s. differences by up to  $0.85 \text{ g kg}^{-1}$ . For wind, the r.m.s. differences are of the order of  $3 \text{ m s}^{-1}$ , with somewhat higher values for Méso-NH versus HIRLAM. Again, as mentioned earlier, no conclusions on possible model deficiencies can be inferred from such an intercomparison, without referring to observations.

(ii) *Validation against sondes.* A rather systematic validation of the mesoscale models against soundings collected during FASTEX was, therefore, carried out for the three studied IOPs. These data included 12-hourly radiosoundings from the conventional observing network, but also enhanced-frequency FASTEX radiosoundings from land stations and ships, as well as dropsoundings performed by the fleet of FASTEX aircraft (Joly *et al.* 1999). The model fields were interpolated at the exact geographical and vertical location of each measurement point, thereby obtaining a set of simulated vertical soundings, valid at simulation times of +6, +9, and +12 hours. For the sake of time consistency, only soundings available within less than one hour from the model forecast times, were retained in the statistical calculations. To further synthesize the results,

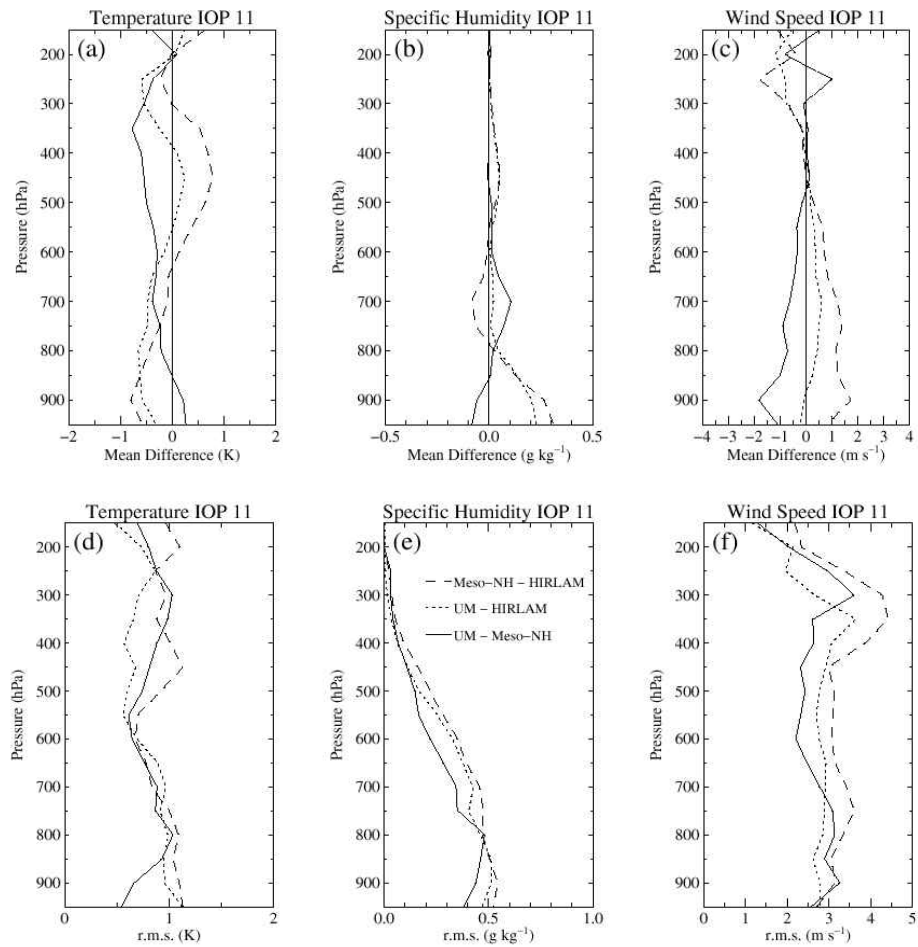


Figure 3. Mean (top) and root mean square (bottom) differences between each pair of mesoscale models, for temperature ((a) and (d)), specific humidity ((b) and (e)), and wind speed ((c) and (f)), for FASTEX IOP 11: UM minus the Meso-NH (solid line), UM minus HIRLAM (dotted line), and Meso-NH minus HIRLAM (dashed line). Units are, respectively, K,  $\text{g kg}^{-1}$ , and  $\text{m s}^{-1}$ . Statistics apply to the 12th hour of the simulation, initiated at 1200 UTC 5 February 1997. See text for explanation of acronyms.

the troposphere was divided into three layers (200–500 hPa, 500–800 hPa, and 800–1000 hPa), in such a way that the available total number of measurements was large enough (several hundred points), and similar among layers. The mean biases and r.m.s. of the deviation model–observation could then be computed. Figure 5 displays the resulting r.m.s. versus bias for the three IOPs and the three models, for the three selected tropospheric layers, and for four observed variables: temperature, specific humidity, wind direction, and wind speed. It should be recalled here that the sonde measurements are assumed to be unbiased, and that their expected accuracy for temperature, wind direction, and wind speed is in the order of 0.5 K, 5 degrees, and  $1 \text{ m s}^{-1}$ , respectively. For specific humidity, it seems reasonable to assume a relative accuracy of about 10%. Bearing these values in mind will help to assess the level of significance of the model versus observation statistics, presented in Fig. 5. Note that in such a validation procedure, based on sparse soundings, differences between model and observations can

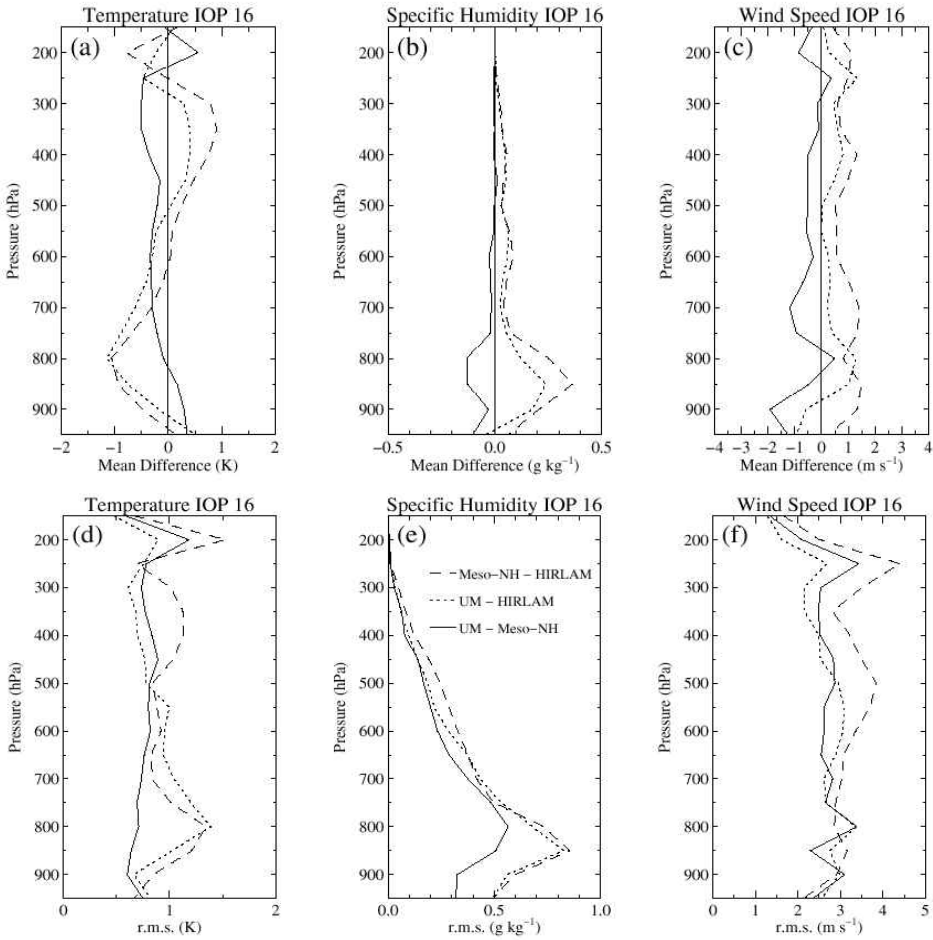


Figure 4. Same as in Fig. 3, but for FASTEX IOP 16. Statistics apply to the 12th hour of the simulation, initiated at 0000 UTC 17 February 1997.

arise from systematic biases, but also from spatial mismatches in regions with strong horizontal gradients.

A careful examination of Fig. 5 clearly points out the main model discrepancies with respect to observations. For the three selected cases, Méso-NH tends to be significantly warmer than the observations in the upper troposphere, while UM and HIRLAM agree with the sondes to better than 0.5 K above 500 hPa. This is consistent with the deviations displayed in Fig. 3(a) and Fig. 4(a). In the 500–800 hPa layer, the model biases are mainly case dependent: cold for IOP 16, and warm for IOP 17. For IOP 11, all models agree with the soundings within 0.5 K. In the lower troposphere, the agreement is also fairly good, except for HIRLAM which exhibits a significant warm bias in the case of IOP 11 and IOP 17. This temperature bias exceeds 1 K for IOP 11, which supports the results of the intercomparison. The specific-humidity biases in the 500–800 hPa layer turn out to be case dependent, all models being significantly too dry for IOP 16, almost neutral for IOP 11, and significantly too moist for IOP 17. Inside the PBL, HIRLAM tends to be slightly too dry, while UM and Méso-NH are usually on the moist side,

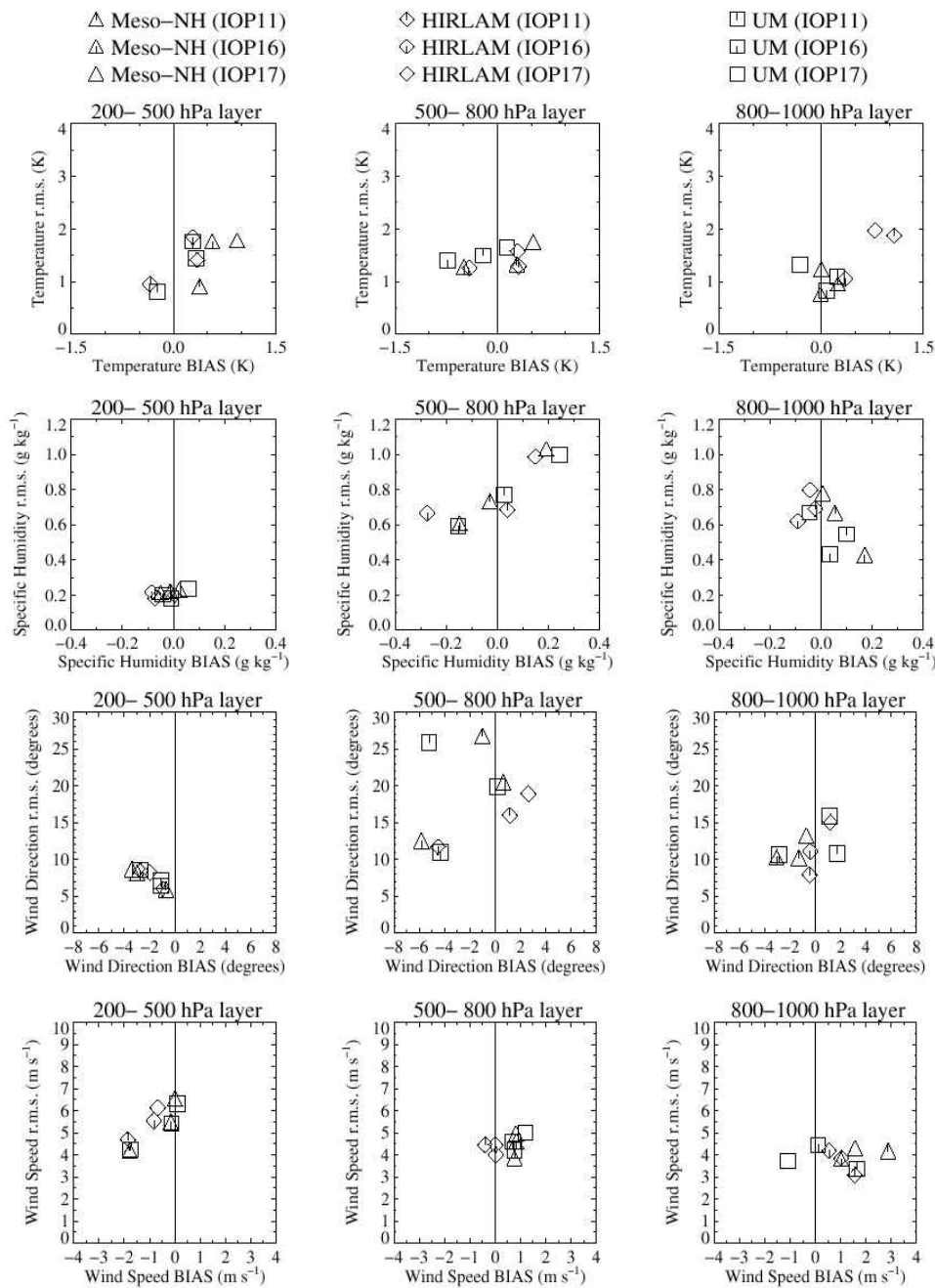


Figure 5. Statistical validation of mesoscale models (see text) against radio- and dropsoundings of temperature (first row), specific humidity (second row), wind direction (third row), and wind speed (fourth row), within three layers of the troposphere: 200–500 hPa (left column), 500–800 hPa (central column), and 800–1000 hPa (right column). Root mean square (r.m.s.) model to observation deviations are plotted versus model–observation mean biases, for Fronts and Atlantic Storm-Track EXperiment Intensive Observing Periods (IOPs) 11, 16 and 17. The main legend indicates the symbols used for each pair of model and IOP.

except for IOP 17. Although the latter biases lie within the observational accuracy, they look consistent with the curves of Fig. 3(b) and Fig. 4(b).

As regards wind direction, the absolute value of the bias is below 6 degrees everywhere for all models. The most significant negative biases are obtained at midlevels for IOP 16 for all three models, as well as for UM in the case of IOP 11. It is worth noticing that the r.m.s. deviations in the midtroposphere are roughly twice as large for IOP 17 as for IOP 16, and even larger for IOP 11 with UM and Méso-NH. The latter difference is attributable to the marked wavy aspect of the midlevel flow in the IOP 11 (see Fig. 1) and IOP 17 (not shown) cases, which implies an enhanced spatial variability of wind direction and, therefore, a higher probability of local mismatches between model and observations.

All models usually underestimate the wind speed in the upper troposphere, very significantly in the IOP 11 case. On the contrary, in the midtroposphere, UM and Méso-NH rather significantly overestimate wind speed by roughly  $1 \text{ m s}^{-1}$ . The three models also tend to over-predict wind velocity inside the PBL, except for IOP 17 with UM, but very significantly in the case of IOP 11. This overestimation inside the PBL may be caused by too low a dissipation of momentum, especially in the presence of strong surface winds as are observed within midlatitude storms. Such deficiencies of current boundary-layer parametrizations at high wind speeds were pointed out by Eymard *et al.* (1999) for instance.

As a summary of this subsection dealing with standard meteorological fields, we can conclude that the three models are in rather good agreement with each other, but also with respect to the radio- and dropsoundings performed during FASTEX. The only systematic and significant deviations between models and observations that can be pointed out are a warm bias in the PBL of HIRLAM, a warm bias in the upper troposphere of Méso-NH, and an overestimation of the wind speed inside the PBL.

### (b) Clouds and precipitation

(i) *Model intercomparison.* One of the main purpose of this mesoscale model intercomparison was to study the representation of cloud and precipitation fields.

A first illustration of the results from the simulations as regards clouds, is given in Fig. 6 which shows the 12-hour forecast vertically integrated amounts of cloud condensate, in the IOP 11 case. The intercomparison is split into two steps: the vertically integrated cloud condensate is first plotted for Méso-NH (a), and HIRLAM (b), then the total content in cloud condensate plus snow is shown for Méso-NH (c), and UM (d). This distinction is necessary because the UM prognostic ice field encompasses both cloud ice and snow. Rain content is not included in this comparison, because it is not a prognostic variable neither in HIRLAM, nor in the UM. The MSLP field is also plotted in Fig. 6.

It should be emphasized here that, aside from possible differences in the dynamics and in the treatment of diffusion, panels (a) and (b) are expected to result from the subtle balance of condensation and ice-to-snow processes, so that differences may be very sensitive to differences in the conversion parametrizations. On the other hand, differences between panels (c) and (d) are expected to be mainly related to differences in the balance between condensation and ice sedimentation. Indeed, the typical values of fall velocity for ice/snow ( $0.5\text{--}1.5 \text{ m s}^{-1}$ ) imply that beyond a spin-up time of 3 hours the total amount of condensate—which mainly consists of ice/snow in the studied cases—is practically governed by the ice sedimentation parametrization used in the model. This was demonstrated by Forbes *et al.* (2000) from simulations of IOP 16 with UM. Both of

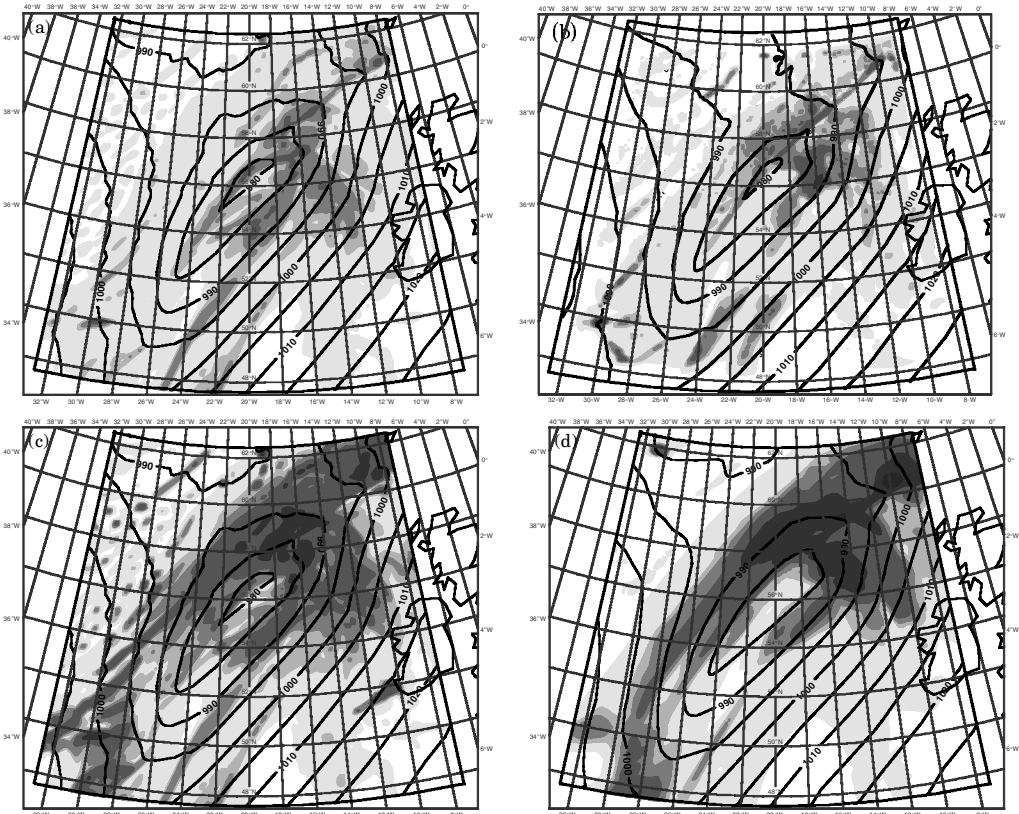


Figure 6. 12-hour forecast total cloud condensate from Méso-NH (a), and HIRLAM (b), and 12-hour forecast total cloud condensate plus snow from Méso-NH (c), and UM (d), for FASTEX IOP 11. Forecast was started at 1200 UTC 5 February 1997. Mean-sea-level pressure is also plotted (isobars every 5 hPa). Isolines correspond to 0.1, 0.3, 0.5, 0.7, 1, 2 and 5  $\text{kg m}^{-2}$ , with a darkening grey shading for values above 0.1  $\text{kg m}^{-2}$ . See text for further explanation.

these processes are uncertain, but ice sedimentation rates are probably better quantified than autoconversion and aggregation/accretion rates.

A comparison of Figs. 6(a) and (b) indicates that the regions of high cloud-condensate amount (up to  $1 \text{ kg m}^{-2}$ ) lie to the north-east of the MSLP minimum in both Méso-NH and HIRLAM. Besides, similar, very narrow cloud bands, are simulated along the axis of the surface trough which corresponds to the south-west to north-east stretching of the MSLP minimum. The two narrow cloud bands that appear in the south of the domain, east of the surface trough, in Méso-NH, are also present in HIRLAM, although they are less sharp. However, some differences can be found between the two maps. Inside the area which is located about 150 km south-east of the low centre, Méso-NH produces cloud condensate amounts that locally exceed  $0.7 \text{ kg m}^{-2}$ , whereas no such pattern is seen in HIRLAM. In addition, although Figs. 1 and 2 suggested a rather good collocation of Méso-NH and HIRLAM warm fronts, the associated Méso-NH cloud pattern is somewhat shifted to the south compared with the HIRLAM one.

When Méso-NH is compared with UM (Figs. 6(c) and (d)) in terms of total cloud condensate plus snow amount, the agreement seems rather satisfactory. In the northern half of the domain, the structure, but also the values, of the simulated fields look rather similar. For instance, the regions with field values larger than  $0.5 \text{ kg m}^{-2}$  are roughly

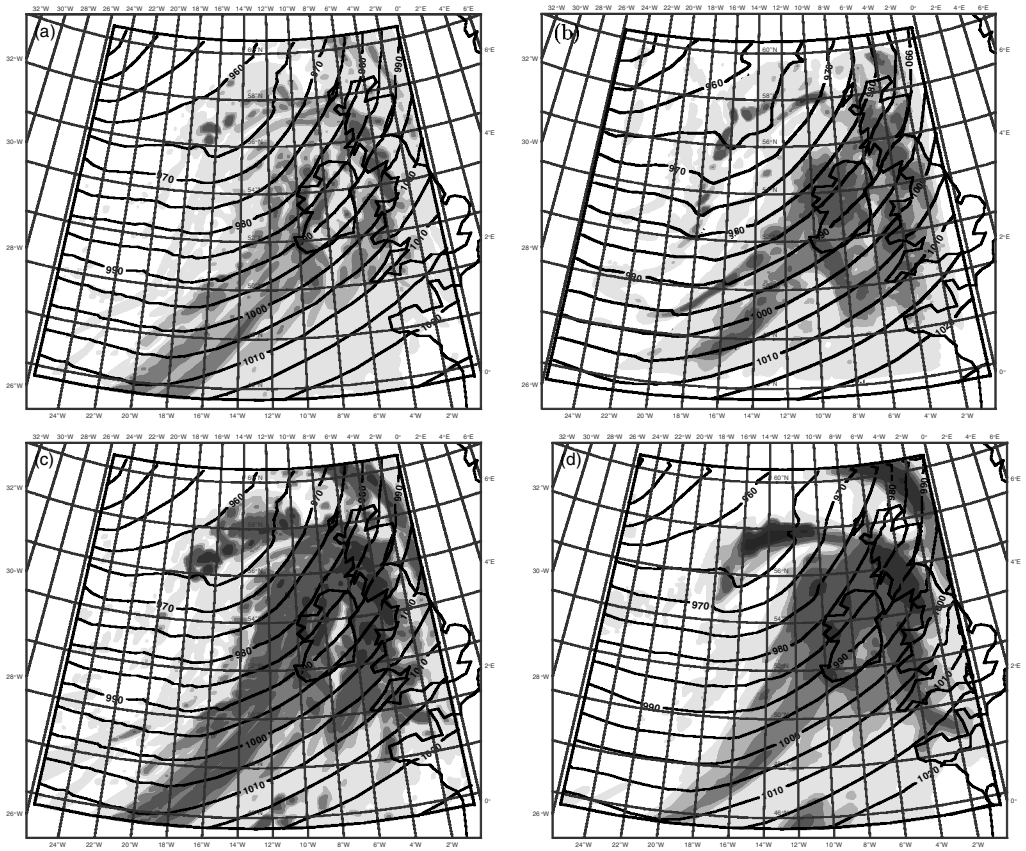


Figure 7. Same as in Fig. 6, but for FASTEX IOP 16. Forecast was started at 0000 UTC 17 February 1997.

collocated. Nonetheless, it should be noted that the highest values attained are larger with UM, than with Méso-NH. In the southern part of the domain, the agreement between the two models is not as good, since, behind the surface trough, Méso-NH has a tendency for generating a series of parallel cloud bands which have the same orientation as the 850 hPa relative-vorticity bands from Fig. 1(b). Such cloud bands are not simulated by UM which produces a smoother and more homogeneous cloud field. Again, this may be partly due to a stronger horizontal diffusion which may remove small-scale variability in UM. Lastly, both Méso-NH and UM simulate a narrow cloud band just ahead of the surface trough, though with higher values in Méso-NH.

Figure 7 displays the same fields as Fig. 6, but for the IOP 16 case. In the same way as for Fig. 6, the fields from panels (a) and (b), on one hand, and from panels (c) and (d), on the other hand, seem to agree fairly well. In particular, the cloud head which was observed during IOP 16 (Forbes *et al.* 2000), is clearly simulated by the three models, but its presence becomes even more conspicuous when one looks at the cloud condensate and snow field, especially with UM. The cloud-free tongue, wedged between the cloud head and the main frontal cloud band, is associated with the dry intrusion which was also well observed during IOP 16 (Forbes *et al.* 2000). It should be underlined that integrated cloud water amounts locally exceed  $5 \text{ kg m}^{-2}$  in the cloud head simulated by UM, but

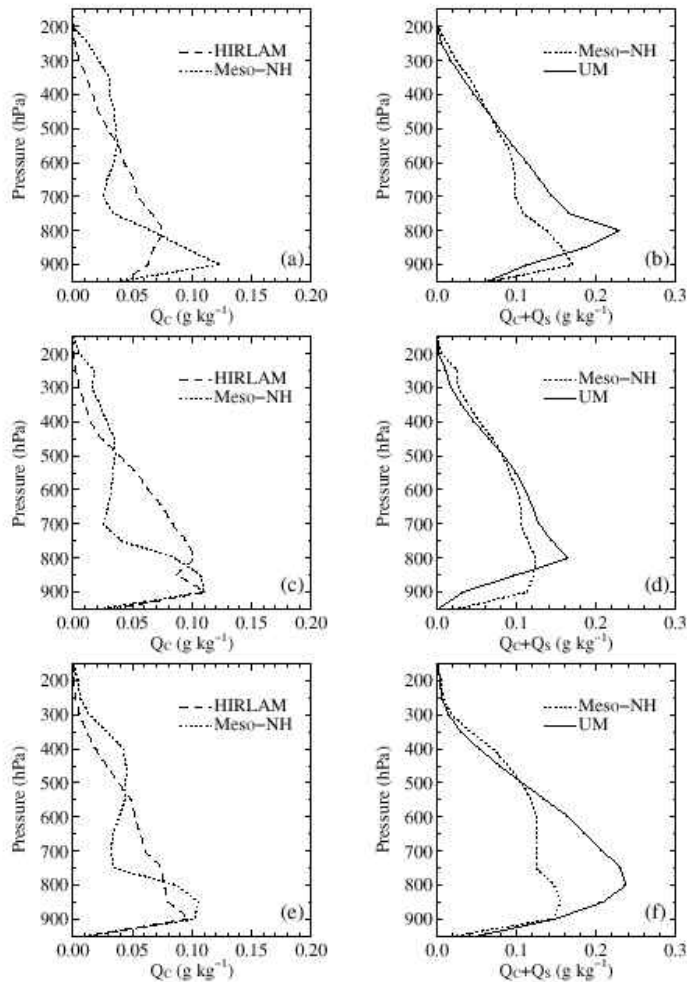


Figure 8. Temporally and spatially averaged vertical profiles of cloud condensate ( $Q_c$ , (a)) and cloud condensate plus snow ( $Q_c + Q_s$ , (b)), for FASTEX IOP 11. Same fields for IOP 16 in (c) and (d), and for IOP 17 in (e) and (f), respectively. Curves for UM, Mésó-NH, and HIRLAM are shown with solid, dotted, and dashed lines, respectively. Contents are expressed in  $\text{g kg}^{-1}$ . See text for explanation of acronyms.

that Mésó-NH produces higher values than UM inside the wide cloud band associated with the trailing cold front.

In addition to this intercomparison of vertically integrated cloud fields, one should also compare the vertical distributions of condensed water/ice. For this purpose, averaged profiles of the 12-hour forecast fields were computed over the entire LAM domain (excluding boundaries). In all three studied cases, the clouds are mainly embedded in the warm sector of the synoptic perturbation. Possible smearing effects associated with the horizontal averaging of signals coming from different altitudes (*especially* freezing effects) should, therefore, remain negligible. It was also checked that the amounts of cloud condensate and surface precipitation in a system-relative framework are almost constant in time after a few hours of integration, which indicates that the model spin-up is already over well before the considered 12-hour forecast range. Figure 8 displays the



resulting vertical profiles of cloud condensate and cloud condensate plus snow for the three IOP cases.

For all IOPs, the condensate profiles show remarkably similar general magnitudes when one considers the markedly different microphysics schemes. However, the profiles from HIRLAM and Méso-NH look substantially different in shape: whereas in HIRLAM, cloud condensate regularly increases downwards, the profile in Méso-NH exhibits a local minimum around 700 hPa. Furthermore, it seems relevant to note that above 500 hPa, the average cloud ice amount is lower in HIRLAM than in Méso-NH.

The values and shapes of the Méso-NH and UM profiles of cloud condensate plus snow are in broad agreement. In the upper troposphere (500–200 hPa) Méso-NH has a little more condensate, while below 500 hPa the UM has more than Meso-NH; the peak also occurs at a slightly higher altitude. Forbes and Clark (2003) show that there are two dominant factors determining the vertical profile of condensate mixing ratio in the region of a system where the terminal fall speed of condensate exceeds the updraught speed. The first is the area-average upward water-vapour flux assuming saturated ascent. This equals, within an additive constant, the area-average downward flux of condensate. The second factor is the average terminal velocity of the condensate. The ratio of these two determines the basic shape of the condensate profile. Other changes in the profile due to the microphysics are only of the order of the supersaturation with respect to ice, typically around 10%.

The different shapes of the mean condensate profile can, therefore, be interpreted as resulting, primarily, either from systematic differences in the underlying dynamics or from differences in the parametrization of terminal velocity. Since Meso-NH has three ice prognostics, the UM one, and HIRLAM a diagnostic split between ice and cloud water, significant differences in the effective terminal velocity are to be expected. As an example, Fig. 9 shows the vertical profiles of domain-averaged frozen condensate flux for Méso-NH and the UM (liquid cloud obviously would contribute nothing to the condensate flux profile, and differences in rainfall flux are of little relevance to this comparison). It is evident that the total flux agrees very well between the models, though a little of the difference suggested in the condensate profile remains. This suggests that gross differences in the underlying dynamics are not contributing to the differences in condensate profile, but rather the different effective fall velocities. The separate components in the Méso-NH scheme are also shown to illustrate the small contribution from ice (which makes up much of the condensate mixing ratio at upper levels) and the significant graupel contribution at lower levels. Similar figures could be shown for the other two cases.

(ii) *Validation against Meteosat.* Meteosat infrared imagery was utilized for the purpose of validating the simulated clouds. As mentioned in section 2(d), the more and more commonly used model-to-satellite approach was adopted, which consisted here of the offline computation of pseudo 10  $\mu\text{m}$ –13  $\mu\text{m}$  Meteosat BTs from the model's state, thanks to Morcrette's radiative-transfer model (1991). Although the assumptions on the ice particle size distributions are of course different in Morcrette's radiative calculations to each of the mesoscale models, Chaboureaud *et al.* (2000) showed that this method could be successfully applied to validating forecasts from Méso-NH. It, therefore, provides a simple and efficient tool for intercomparing our three mesoscale models. The major limitation of its applicability in the present case occurs in regions of strong convection, since the convective clouds which are diagnosed by the models, are not allowed to impact directly on the BT retrievals. In extratropical cyclones, the validation procedure should, therefore, be performed outside the unstable cold air masses that are

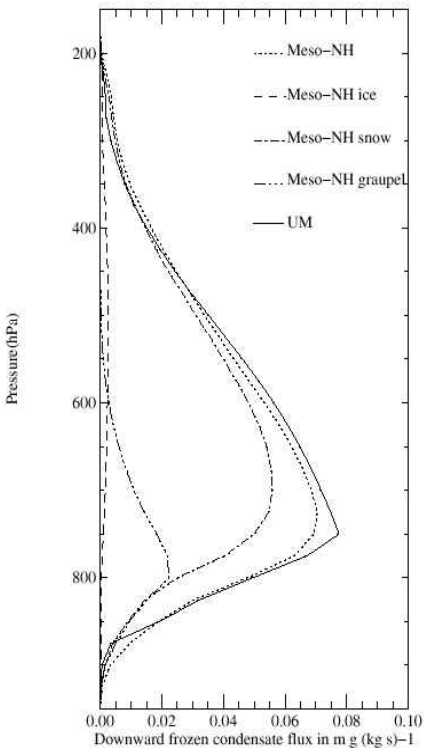


Figure 9. Temporally and spatially averaged vertical profiles of the downward flux of frozen condensate for FASTEX IOP 16. Curves for UM and Mésó-NH are shown with solid and dotted lines, respectively. The contributions from ice, snow and graupel to the total flux are also shown for Mésó-NH with linestyles as indicated in the legend. Contents are expressed in  $(\text{m g}) (\text{kg s})^{-1}$ . See text for explanation of acronyms.

located in the wake of the main stratiform cloud system. It may also be relevant to recall that IR BTs are strongly and negatively correlated with the cloud-top heights.

Figure 10 gives a comparison of the 12-hour simulated IR BTs, as retrieved from the mesoscale models, with the values observed by Meteosat in the IOP 11 case. The mean model–satellite BT biases are equal to +1.5, –11.5 and +10.2 K, for UM, Mésó-NH and HIRLAM, respectively. These biases, together with a visual comparison of the plots, indicate that UM agrees well with the satellite measurements, while Mésó-NH cloud tops extend too high. On the other hand, HIRLAM suffers from a systematic overestimation of BTs. This latter result is consistent with Fig. 8, and suggests that the actual upper-level cloud condensate should lie in between the HIRLAM and Mésó-NH values. The more speckled aspect of HIRLAM BTs is attributed to the combination of the higher spatial variability of the vertical velocity in this model with the use of a diagnostic cloud scheme which implies a more direct response of the cloud fields to the dynamics.

Figure 11 displays simulated and observed BTs for IOP 16. The corresponding mean model–satellite BT biases are equal to +4.7, –0.9 and +8.4 K. For this case, UM and again HIRLAM tend to over-predict BTs, while on average Mésó-NH values match the observations very nicely. One can also note that the western side of the simulated cloud head is correctly located, whereas its eastern edge lies too far away from the polar-front cloud band in the models.

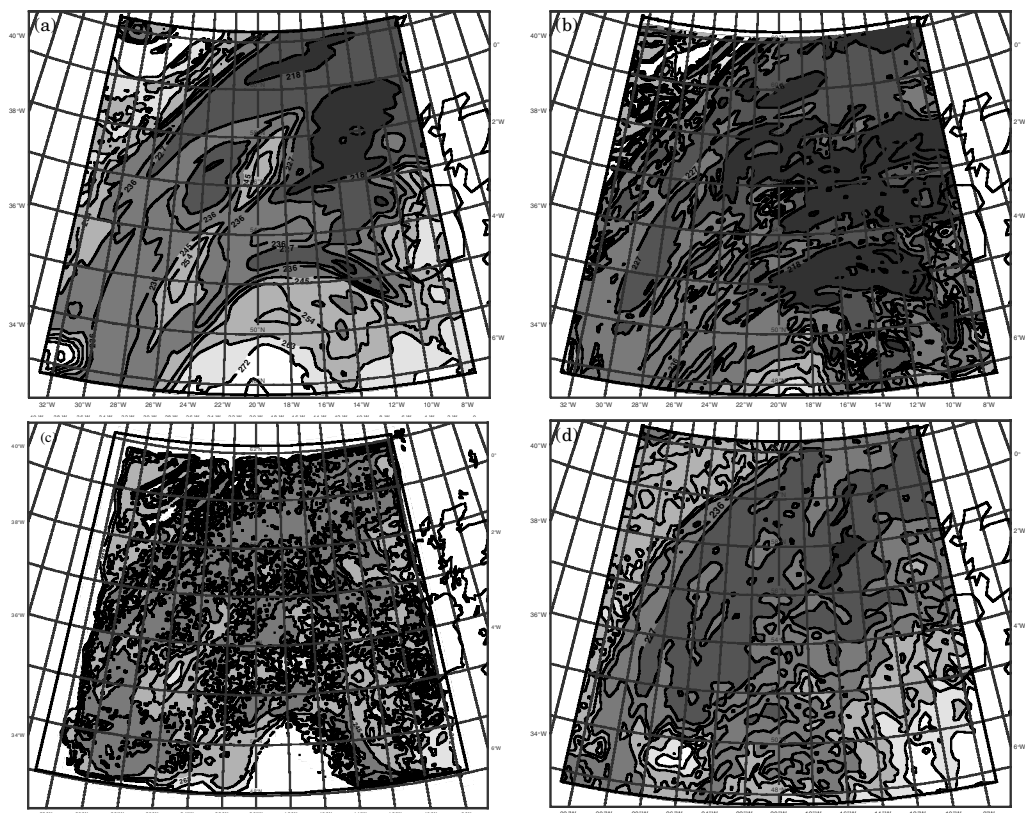


Figure 10. Validation of simulated infrared BTs from UM (a), Méso-NH (b), and HIRLAM (c), against Meteosat observed values (d), for FASTEX IOP 11, at 0000 UTC 6 February 1997. Isolines are drawn every 9 K, darker shading corresponds to colder BTs, and white areas indicate BTs larger than 272 K. See text for explanation of acronyms.

(iii) *Validation against observed surface precipitation.* As the IOP 16 simulation domain encompassed Ireland and part of Great Britain, precipitation measurements from ground stations were used for validating the forecast 6-hour accumulated rainfall at 1200 UTC 17 February 1997. Data were available from 144 stations, distributed rather homogeneously over land. In order to make the comparison easier, the approach of interpolating the 11 km modelled precipitation field at each observation location was adopted, which yielded 144 simulated rainfall values.

Figure 12 shows the frequencies of the 6-hourly surface rainfall values for the station observations and for the three mesoscale models. For all models there are too few points with precipitation lower than 1 mm. This lack of very light precipitation is more pronounced in HIRLAM and UM than in Méso-NH. On the contrary, the frequency of occurrence of rainfall amounts between 1 and 5 mm is higher in the simulations than in the observations. The frequency of occurrence of moderate precipitation (5–10 mm) matches the observations with HIRLAM, is overestimated in UM and clearly underestimated in Méso-NH. Rainfall amounts between 10 and 15 mm are more frequent in all three models than observed. Lastly, the number of points with heavy precipitation (higher than 15 mm) in HIRLAM is very close to the observed number, while UM and Méso-NH have too few of them.

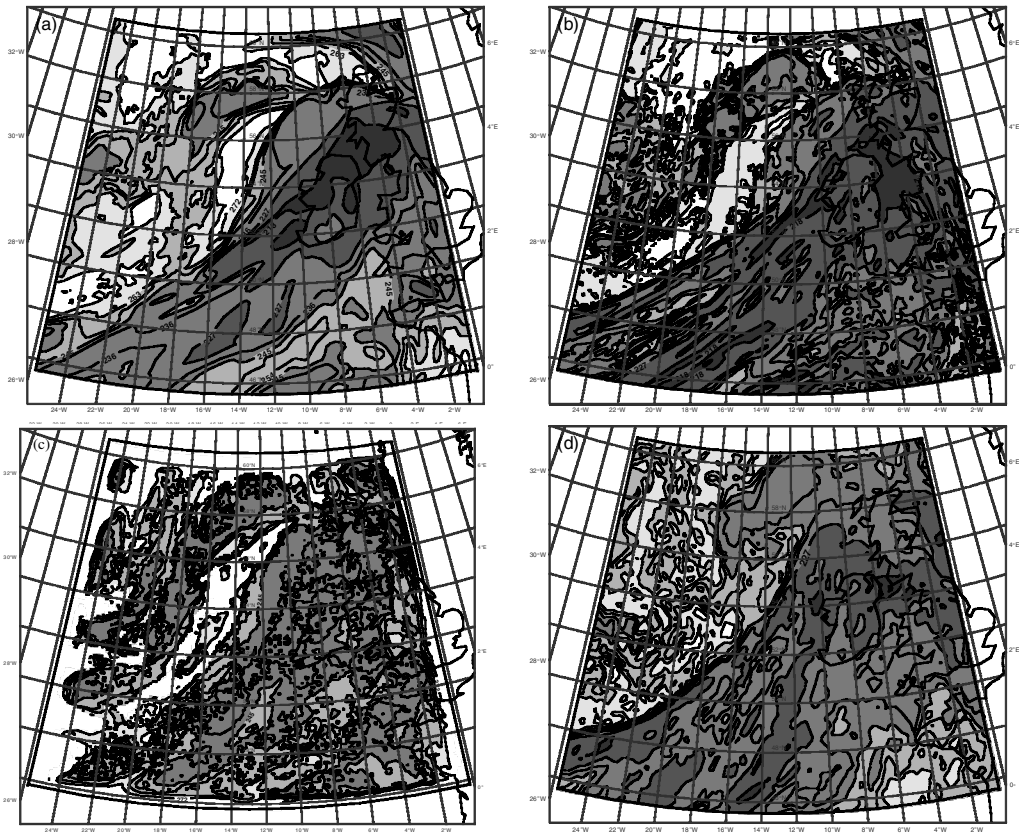


Figure 11. Same as in Fig. 10, but for FASTEX IOP 16, at 1200 UTC 17 February 1997.

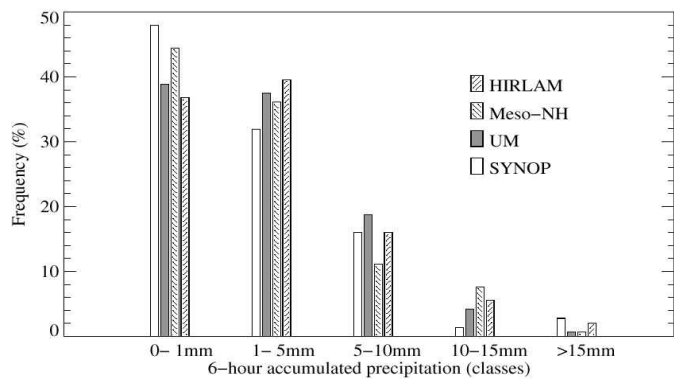


Figure 12. Frequency distributions of the 6-hour accumulated rainfall amounts from observations (SYNOP) and from each one of the mesoscale models, at 1200 UTC 17 February 1997 (FASTEX IOP 16). Five classes of precipitation values are considered here. See text for explanation of acronyms.

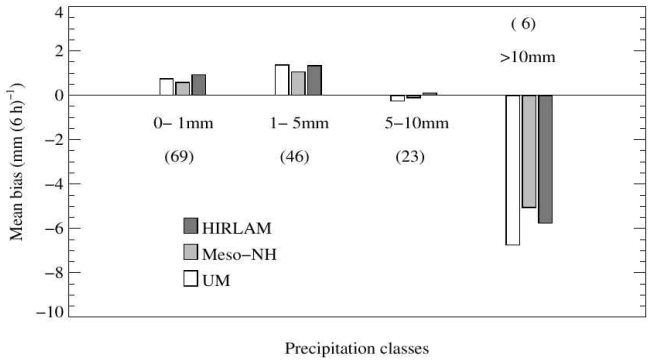


Figure 13. Model–observation mean biases for four classes of observed 6-hour accumulated precipitation amounts, at 1200 UTC 17 February 1997 (FASTEX IOP 16): UM (white), Mésos-NH (grey), and HIRLAM (dark grey). Precipitation ranges are reported below or above the corresponding bars, and the number of observations in each class is indicated in parentheses. Biases, are expressed in mm per 6 hours. See text for explanation of acronyms.

Since the frequency distribution of Fig. 12 cannot account for the spatial distribution of the rainfall values, the model–observation mean biases were also computed for four classes of observed precipitation amounts, and are displayed in Fig. 13. From this figure, it is obvious that all models overestimate precipitation below 5 mm, which is consistent with the widening of the models probability density function (PDF) distributions in Fig. 12. Between 5 and 10 mm, no systematic bias is found in the simulated precipitation. Lastly, the heaviest observed rainfall amounts seem to be dramatically under-predicted by the three models. This result is in agreement with the lower frequencies of the simulated precipitation above 15 mm in Fig. 12. A larger statistical sample would help to confirm this finding. As a summary, Fig. 12 and Fig. 13 suggest that the models do not produce enough extreme low or high precipitation, compared with observations.

(iv) *Validation against airborne-radar data.* Several attempts were made to validate high-resolution simulations of the studied FASTEX cases that were obtained with the ARPEGE model, against the airborne X-band-radar data. The comparison was applied to horizontally and temporally averaged quantities in order to filter out the natural variability of the radar data.

The first method consisted of a comparison of the precipitation contents of the model with equivalent measurements that were retrieved by the CETP\* from the combined radar and dropsonde data. At all vertical levels available, the simulated precipitation contents turned out to be about twice as large as the radar retrievals.

The alternative approach of comparing the radar reflectivities with values calculated from the model state, led to the conclusion that the radar and model reflectivities agreed within a couple of dBZ inside rainy layers, but exhibited a negative bias at snowy levels which increased with height (up to  $-10$  dBZ at 5500 m).

In view of the contradictory results of the two approaches, it seems impossible to draw any clear conclusion on the correctness of the 3D precipitation contents that are given by the models. The difficulty in reaching a conclusion is also enhanced by the high uncertainty in the 3D precipitation retrievals from the radar (first approach), as

\* Centre d'études des Environnements Terrestres et Planétaires, Vélizy, France.

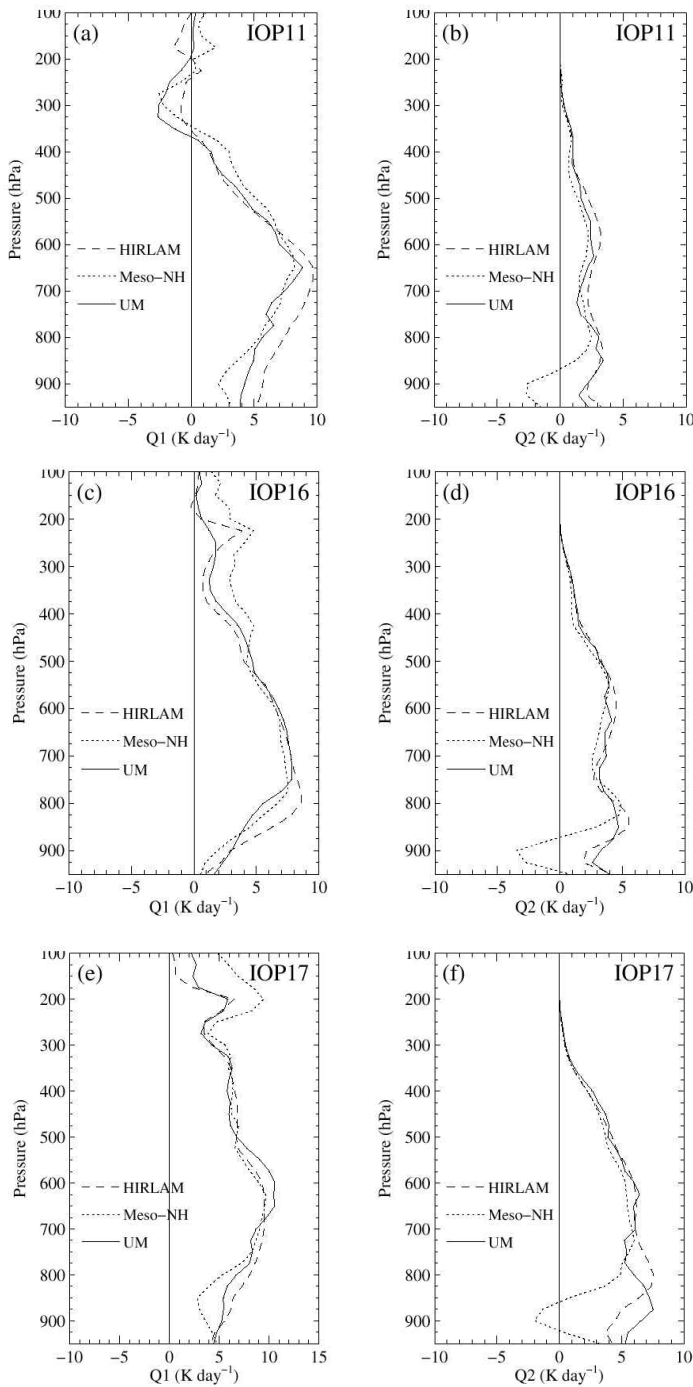


Figure 14. Vertical profiles of apparent heat source ( $Q_1$ ) and apparent moisture sink ( $Q_2$ ), as computed from UM (solid), Méso-NH (dotted), and HIRLAM (dashed), over the last 6 hours of each mesoscale simulation. Panels (a) and (b):  $Q_1$  and  $Q_2$  for FASTEX IOP 11; (c) and (d):  $Q_1$  and  $Q_2$  for IOP 16; (e) and (f):  $Q_1$  and  $Q_2$  for IOP 17. Heating rates are expressed in K day<sup>-1</sup>. See text for explanation of acronyms.

well as by the questionable validity of the assumptions on particle number and size distributions which need to be made for calculating the reflectivities from the model (second approach).

These are the reasons why no quantitative validation of the mesoscale simulations against radar data is shown in this paper.

### (c) *Heat and moisture budgets*

The apparent heat source and the apparent moisture sink, respectively denoted  $Q_1$  and  $Q_2$ , provide a good way for estimating the sensible and latent heating of the atmosphere due to all processes that are parametrized in a given model (e.g. Redelsperger *et al.* 2000). In other words, these two quantities are equal to the sum of the contributions from large-scale and convective condensation, radiation (only in  $Q_1$ ), and subgrid-scale vertical and horizontal turbulent mixing. In this study,  $Q_1$  and  $Q_2$ , which were computed from the output of each mesoscale model, were based on spatial averages over the entire integration domain (excluding boundary zones), and over the time interval between forecast times +6 and +12 hours.

Figure 14 displays the vertical profiles of  $Q_1$  and  $Q_2$  for the three IOP cases and for the three models. As regards  $Q_1$ , the profiles look rather analogous from the surface up to 400 hPa, with a global heating of the bottom half of the troposphere. A similar peak value between 8 and 10 K day<sup>-1</sup> is found in all cases, with a good agreement between models as regards its location in the vertical, for all IOPs. Above 400 hPa, larger differences are seen between the three models. As far as  $Q_2$  is concerned, profiles from all three models look very close from the top of the troposphere down to 800 hPa, for all IOPs, and show the heating due to condensation. Below 800 hPa, Méso-NH exhibits a behaviour which is dramatically different from the two other models, for all IOPs. Indeed, although the three profiles are comparable in shape, the first kilometre just above the surface is characterized by negative values of  $Q_2$  in Méso-NH, but positive values in HIRLAM and UM. Further investigations into this specific issue attributed this discrepancy to the parametrization of turbulence which is fundamentally different in Méso-NH with respect to UM and HIRLAM. The reason why a turbulent scheme gives different results from the two others is beyond the scope of this paper. Besides, there is no indication that the discrepancy in  $Q_2$  is able to feedback on the moisture fields on the 12-hour time-scale considered here.

## 4. UPSCALING OF MESOSCALE SIMULATIONS

For the purpose of addressing the questions formulated in the introduction, an attempt was made to check whether a coarse-resolution AGCM is able to simulate large-scale fields which are consistent with the results from the high-resolution runs, averaged to the AGCM resolution (called ‘upscaled’, in the following).

Since the resolution in climate models is currently close to 300 km, the ARPEGE AGCM was run with a corresponding T42 spectral truncation, starting from the same initial conditions as in the mesoscale runs. Given that calculations which were performed on FASTEX IOP 11 and IOP 16 led to similar results, we will focus here on the IOP 16 simulation.

As a first step, the outputs from the mesoscale runs were averaged over a 300 km grid made of  $5 \times 5$  boxes. The value of each meteorological field inside each one of these 25, 300 km  $\times$  300 km boxes was defined as the spatial average over the  $28 \times 28$  original mesoscale grid points contained in the coarse-resolution box. Note that the lateral boundary zones, where the relaxation of the LAM fields is active, were excluded

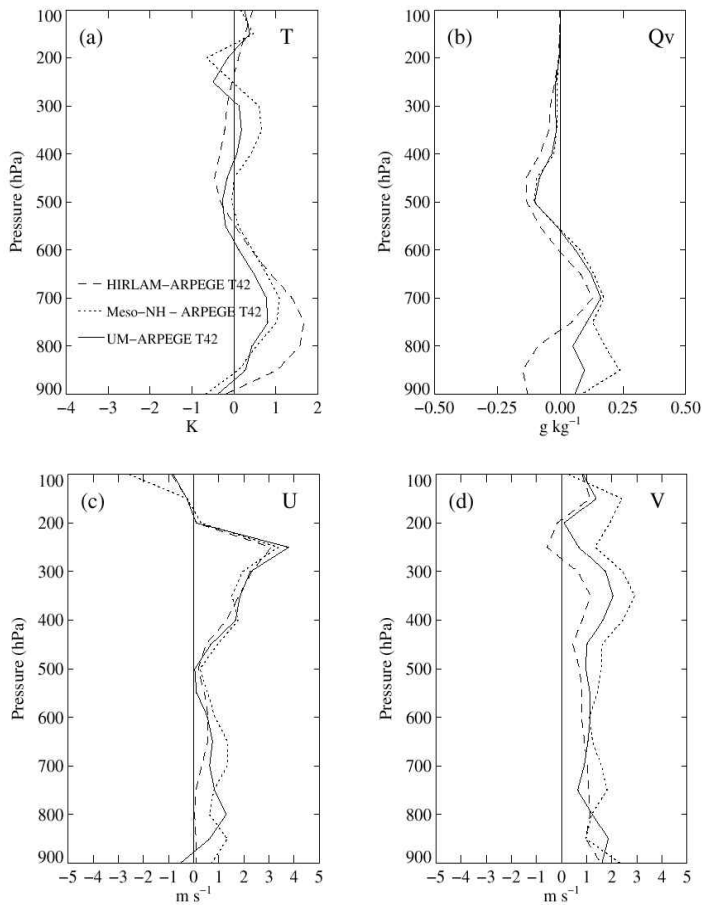


Figure 15. Domain-averaged vertical profiles of the deviation between the upscaled, 12-hour forecast mesoscale fields and the corresponding outputs from the ARPEGE run (see text), at 300 km resolution, for temperature (a), specific humidity (b), zonal wind (c), and meridional wind (d). Curves are shown for UM (solid), Mésó-NH (dotted), and HIRLAM (dashed), and for FASTEX IOP 16. Units are indicated at the bottom of each plot. See text for explanation of acronyms.

from these calculations. The outputs from ARPEGE were also interpolated at the 25 points of the 300 km grid.

Figure 15 displays the vertical profiles of the deviations between the upscaled mesoscale models and the ARPEGE AGCM, averaged over the entire coarse grid, for the 12-hour forecast temperature, specific humidity, zonal wind and meridional wind, in the IOP 16 case. The three mesoscale models exhibit rather comparable deviations with respect to the coarse-resolution AGCM for temperature and the two components of the wind. They are clearly warmer between 600 hPa and the surface, and they generate stronger winds at all levels, in particular around the tropopause (excess of up to 4 m s<sup>-1</sup>). In terms of specific humidity, the deviations are very similar down to 700 hPa, but contrary to UM and Mésó-NH, HIRLAM is drier than the AGCM inside the PBL.

In addition to the domain-averaged deviations presented in Fig. 15, it also seems important to study the degree of spatial homogeneity of these departures, and in particular to determine whether they depend on the location inside the cloud system. First, Fig. 16 displays various 12-hour forecast fields from the upscaled mesoscale simulations and



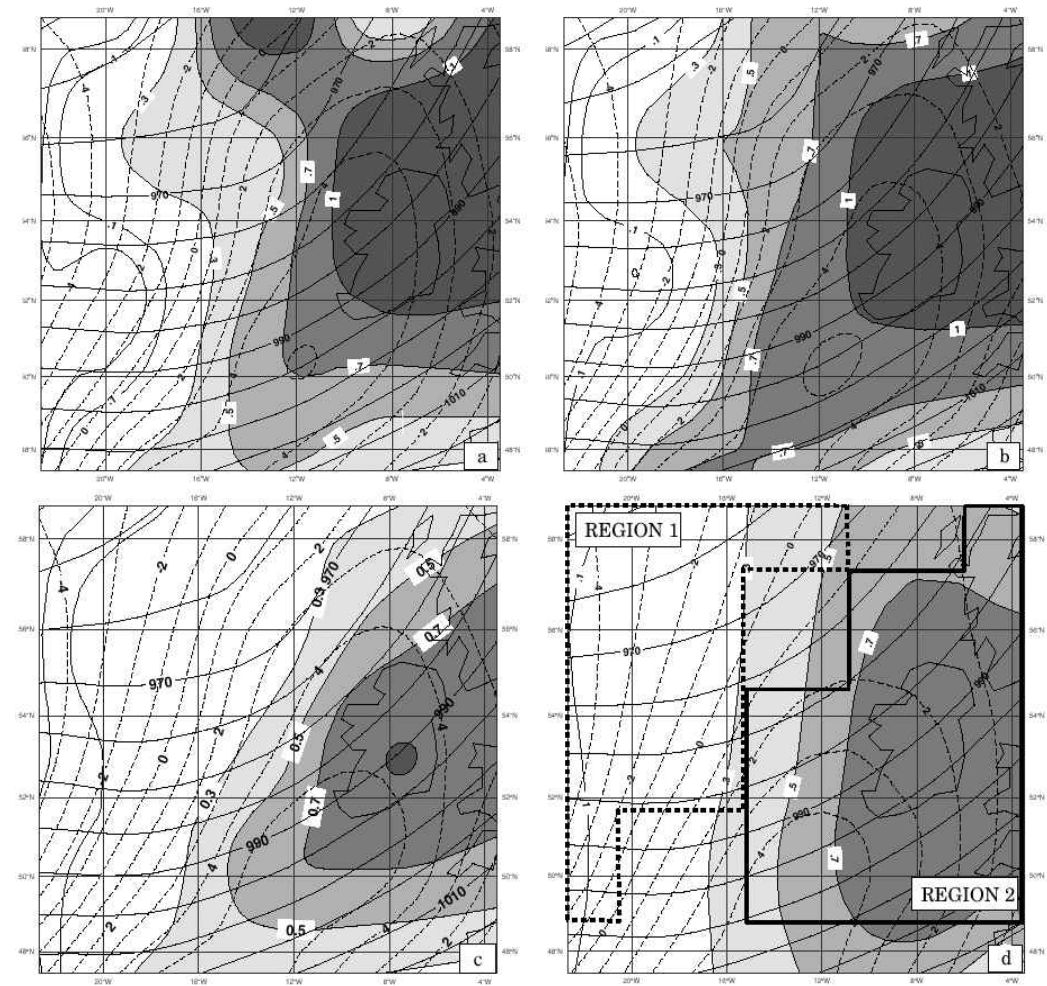


Figure 16. 12-hour forecast vertically integrated condensate amount (grey shading), 850 hPa temperature (thin dashed lines), and mean-sea-level pressure (thin solid lines), from the upscaled runs with UM (a), Méso-NH (b), and HIRLAM (c), and from the 300 km resolution ARPEGE run (d), for IOP 16 at 1200 UTC 17 February 1997. The thick dashed and solid lines in (d) respectively delimit regions 1 and 2 mentioned in the text. The isolines for condensate are plotted for 0.05, 0.1, 0.3, 0.5, 0.7 and 1 kg m<sup>-2</sup>. Isotherms are shown every 1 °C, and isobars every 2.5 hPa. See text for explanation of acronyms.

from the 300 km ARPEGE run. The superimposed fields are the vertically integrated condensate amount, which includes snow in all cases except HIRLAM, the 850 hPa temperature, and the MSLP. The structures of the temperature and MSLP fields look rather comparable in all simulations, although the MSLP low seems somewhat deeper (by about 3 hPa) and the warm sector more pronounced in the three mesoscale models than in the AGCM. The comparison of panels (a), (b) and (c) with panel (d) suggests that the cloud system which is simulated with ARPEGE at coarse resolution agrees fairly well with the cloud system obtained with the high-resolution models. Therefore, the primary generation of large-scale cloud and precipitation seems to be properly resolved in the AGCM, even though the condensate amounts are a little lower in the AGCM than in UM and Méso-NH. One should keep in mind here that the HIRLAM condensate does not include snow and cannot, therefore, be quantitatively compared with the field values from the other models. It is worth noticing that even after the upscaling procedure, some

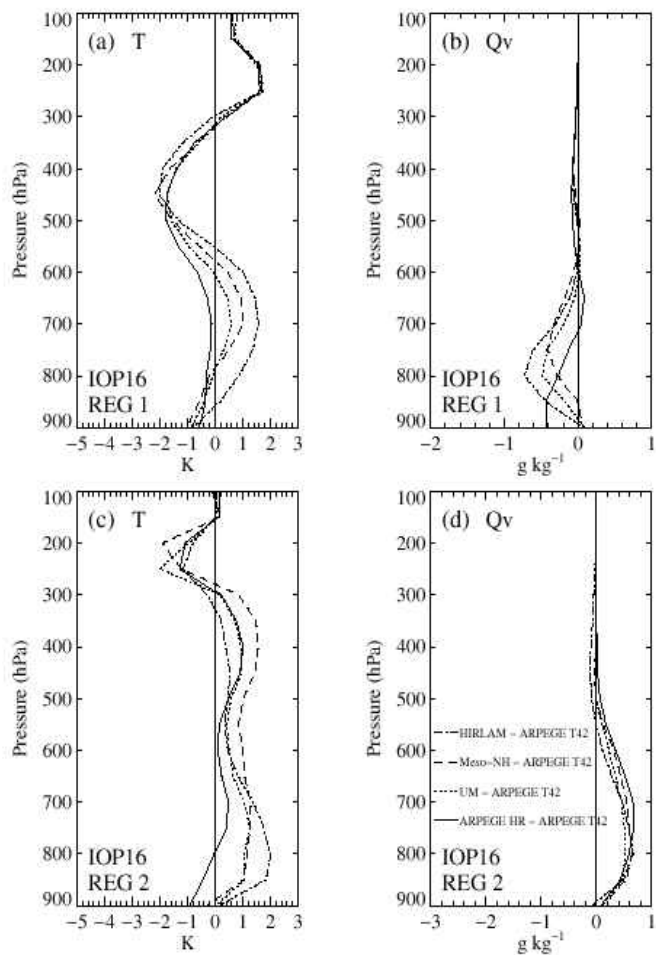


Figure 17. Vertical profiles of the deviations between the upscaled mesoscale models and the 300 km resolution ARPEGE atmospheric general-circulation model, averaged over region 1 for temperature (a) and specific humidity (b), and over region 2 for temperature (c) and specific humidity (d). Regions 1 and 2 were defined in Fig. 16(d), and profiles are shown for UM–ARPEGE (dot), Méso-NH–ARPEGE (dash), and HIRLAM–ARPEGE (dot-dash), for the IOP 16 case at 1200 UTC 17 February 1997. Also shown is the comparison of a 20 km ARPEGE simulation with the 300 km ARPEGE reference run (solid). Temperature deviations are in kelvin, and specific humidity deviations  $\text{g kg}^{-1}$ . See text for explanation of acronyms.

remnants of the IOP 16 cloud head are present in UM, and to a lesser extent in Méso-NH as well, which cannot be found in the AGCM run. This suggests that some contributions from subgrid-scale processes are still not adequately parametrized in the latter model, in particular the generation of precipitation in the cloud head which involves small-scale frontogenesis. It is, however, not clear how the effects of such unresolved frontogenesis should be parametrized. Given that there is no significant spatial shift between the temperature, MSLP, and cloud main patterns, it becomes possible to compute averages over sub-domains of the cloud system that are meteorologically comparable among the models. A preliminary study of the 25 individual boxes of the 300 km grid has led to the definition of the two regions shown in Fig. 16(d), which respectively correspond to the eastern wake of the system characterized by cold and dry air (region 1, encompassing eight boxes), and to its warm and cloudy sector (region 2, encompassing nine boxes).

Vertical profiles of the region-averaged deviations between each upscaled mesoscale model and the ARPEGE AGCM are plotted in Fig. 17 for temperature and specific humidity over both regions. Figure 17 points out totally different departures for both temperature and specific humidity inside the two regions of the cloud system. The deviations between a 20 km run with ARPEGE (local resolution over the IOP 16 domain) and the ARPEGE 300 km simulation are also plotted to help estimate to what extent the biases are due to differences in the models parametrizations or rather to some systematic deficiencies in the representation of subgrid-scale processes at coarse resolution.

In the cold and dry region (region 1), all upscaled mesoscale models are colder than the coarse AGCM inside the PBL, warmer between 600 and 800 hPa, substantially colder between 300 and 600 hPa, and warmer again above 300 hPa. At the same time, the three mesoscale models are significantly drier than ARPEGE below 600 hPa, with a maximum negative departure at the top of the PBL (around 800 hPa). In the warm and cloudy sector (region 2), the mesoscale models are warmer than ARPEGE between the surface and 300 hPa, moister between the surface and 500 hPa, and have larger cloud condensate amounts (see Fig. 16). This is consistent with the fact that the mesoscale models have stronger ascents in the midtroposphere (not shown) than the large-scale AGCM. From 300 hPa up to 150 hPa, the mesoscale models get colder than the AGCM, which is the result of an enhanced radiative cooling at cloud tops in the former models. It is worth noticing that the profiles which were also computed over the cloudy region of IOP 11 (not shown), turned out to be very close to the profiles of Figs. 17(c) and (d). One should note that the deviations in the case of the ARPEGE high-resolution simulation are comparable to the ones obtained for the mesoscale models. This is particularly true for temperature above 500 hPa as well as for specific humidity at all levels. One can, therefore, conclude that the deviations do not originate from differences among models. The fact that the shapes of the deviation curves differ so much in the two highly dissimilar regions 1 and 2, suggests the existence of some systematic deficiencies in the coarse AGCM that strongly depend on the occurrence of thick layer clouds. Future work should first aim to isolate which processes are responsible for these deficiencies in both cloud-free and cloudy regions. Then, one should try to determine whether these deviations could be cured by a mere retuning of the AGCM parameters, or whether they are due to either inadequate parametrizations or a missing representation of some subgrid-scale processes in the model.

## 5. CONCLUSIONS

Three FASTEX synoptic cloud systems were simulated over 12 hours with three mesoscale models, at an 11 km horizontal resolution and with between 45 and 52 vertical levels. A rather good coherence was found between the models, as regards the spatial structure of the dynamical fields, with the simulation of the same main vorticity bands, and similar MSLP patterns. The intercomparison of the three models and their individual validation against radio- and dropsoundings, underlined their rather similar behaviours. However, a better agreement was found in the comparison of UM and Méso-NH versus Meteosat BTs. The validation against sondes also indicated an overestimation of wind speeds in the lowest 2 kilometres, for all models, which may advocate a slight retuning of their parametrizations of the vertical transport of momentum inside the planetary boundary layer. The comparison of the simulated precipitation amounts with rain-gauge observations showed that the three mesoscale models tend to underestimate both very weak and very high rainfall amounts, while moderate precipitation ( $5\text{--}10\text{ mm (6 hours)}^{-1}$ ) is rather well forecast.

The comparison of the upscaled mesoscale fields, taken as a reference, with corresponding outputs from the ARPEGE AGCM run at a climate-like horizontal resolution, allowed it to be pointed out that the AGCM 'biases' depend on the location inside the cloud system, with for instance, totally different vertical profiles inside the warm cloudy sector and the cold dry wake. Further efforts should be dedicated to the detection and understanding of these systematic AGCM deficiencies in coarse-resolution simulations of other typical meteorological events. Then, the retuning of already implemented parametrizations or the development of new ones should eventually help to improve the results of climate models.

It seems also very interesting to underline that in spite of the dramatically different formulations of the models used in this study (hydrostatic versus non-hydrostatic, limited-area versus global, different parametrizations of microphysics and turbulent mixing), rather coherent results were obtained with all models. The differences between the mesoscale models would probably become larger if the simulations were run over a longer period of time, but their spatial structure would be similar as indicated by preliminary 18-hour simulations with UM. However, the coherence found among the mesoscale models is confirmed by the remarkable similarity of the derived 'biases' in the low-resolution AGCM, which suggests that these biases are a robust demonstration of an absence of treatment of some unresolved processes, like small-scale frontogenesis.

#### ACKNOWLEDGEMENTS

The present study was achieved as part of the FASTEX-CSS project, funded by the European Union under contract number PL970235. Part of this work was also supported by Institut National des Sciences de l'Univers/Programme Atmosphère et Océan à Moyenne Échelle, and computer resources of Laboratoire d'Aérodynamique were provided by Centre Nationale de la Recherche Scientifique/Institut du Développement et des Ressources en Informatique Scientifique (project number 1076). Special thanks should be addressed to the Centre National de Recherches Météorologiques/Groupe de Météorologie de Moyenne Echelle/Recherches et Expérience sur les CYclogénèse et les Fronts team from Météo-France, for their scientific and technical support. We are also very grateful to Richard Forbes (JCMM) who provided the surface precipitation observations over the British Isles, and to Jean-Jacques Morcrette (European Centre for Medium-Range Weather Forecasts) who made it possible for us to utilize his Meteosat radiative-transfer model. The three anonymous reviewers should also be thanked for their constructive comments which were very helpful for improving the form and the content of this paper.

#### REFERENCES

- |   |      |  |
|---|------|--|
| Arbogast, P. and Joly, A.   | 1998 | Identification des précurseurs d'une cyclogénèse. <i>C.R.A.S. Paris/Earth &amp; Planetary Sciences</i> , <b>326</b> , 227–230      |
| Baehr, C., Pouponneau, B.,<br>Ayrault, F. and Joly, A.                    | 1999 | Dynamical characterization of the FASTEX cyclogenesis cases. <i>Q. J. R. Meteorol. Soc.</i> , <b>125</b> , 3469–3494               |
| Bechtold, P., Bazile, E.,<br>Guichard, F., Mascart, P. and<br>Richard, E. | 2000 | A mass-flux convection scheme for regional and global models. <i>Q. J. R. Meteorol. Soc.</i> , <b>127</b> , 1–18                   |
| Bougeault, P.   | 1985 | A simple parameterization of the large-scale effects of cumulus convection. <i>Mon. Weather Rev.</i> , <b>113</b> , 2108–2121      |
| Bougeault, P. and Lacarrère, P.   | 1989 | Parameterization of orographically induced turbulence in a mesobeta-scale model. <i>Mon. Weather Rev.</i> , <b>117</b> , 1872–1890 |

- Bougeault, P., Bélair, S., Carrière, J.-M., Cuxart, J., Ducrocq, V., Fischer, C., Hénil, C., Lafore, J.-P., Mascart, P., Masson, V., Pinty, J.-P., Richard, E. and Stein, J. 1999 'The Méso-NH atmospheric simulation system'. Scientific documentation Tech. report. Météo-France/CNRM/GMME, Toulouse, France
- Cammas, J.-P., Poupponneau, B., Desroziers, G., Santurette, P., Joly, A., Arbogast, P., Mallet, I., Caniaux, G. and Mascart, P. 1999 FASTEX IOP17 cyclone: Introductory synoptic study with field data. *Q. J. R. Meteorol. Soc.*, **125**, 3393–3414
- Carpenter, K. M. 1982 Note on the paper 'Radiation conditions for lateral boundaries of limited area numerical models'. *Q. J. R. Meteorol. Soc.*, **108**, 717–719
- Chaboureau, J.-P., Cammas, J.-P., Mascart, P., Pinty, J. P. and Claud, C. 2000 Evaluation of a cloud system life-cycle simulated by Méso-NH during FASTEX using METEOSAT radiances and TOVS-31 cloud retrievals. *Q. J. R. Meteorol. Soc.*, **126**, 1735–1750
- Chen, C. 1991 A nested grid non-hydrostatic, elastic model using a terrain-following coordinate transformation: The radiative-nesting boundary conditions. *Mon. Weather Rev.*, **119**, 2852–2869
- Courtier, P., Freydlér, C., Geleyn, J.-F., Rabier, F. and Rochas, M. 1991 'The ARPEGE project at Météo-France'. Pp. 193–231 in Proceedings of the ECMWF workshop on numerical methods in atmospheric models, September 1991, ECMWF, Reading, UK
- Cullen, M. J. P. 1993 The unified forecast/climate model. *Meteorol. Mag.*, **122**, 81–94
- Davies, H. C. 1976 A lateral boundary formulation for multi-level prediction models. *Q. J. R. Meteorol. Soc.*, **102**, 405–418
- Desroziers, G., Poupponneau, B., Thépaut, J.-N., Janisková, M. and Veersé, F. 1999 Four-dimensional variational analyses of FASTEX situations using special observations. *Q. J. R. Meteorol. Soc.*, **125**, 3339–3358
- Durran, D. 1989 Improving the anelastic approximation. *J. Atmos. Sci.*, **46**, 1453–1461
- Eymard, L., Caniaux, G., Dupuis, H., Prieur, L., Giordani, H., Troadec, R., Bessemoulin, P., Lachaud, G., Bouhours, G., Bourras, D., Guérin, C., Le Borgne, P., Brisson, A. and Marsouin, A. 1999 Surface fluxes in the North Atlantic current during CATCH/FASTEX. *Q. J. R. Meteorol. Soc.*, **125**, 3563–3599
- Forbes, R. M. and Clark, P. A. 2003 Sensitivity of extratropical cyclone mesoscale structure to the parametrization of ice microphysical processes. *Q. J. R. Meteorol. Soc.*, **129**, in press
- Forbes, R. M., Lean, H. W., Roberts, N. M. and Clark, P. A. 2000 'Implications for mesoscale modelling from a study of the FASTEX IOP 16 mid-latitude cyclone'. Tech. Report 302, JCOMM 2000
- Gal-Chen, T. and Somerville, R. C. J. 1975 On the use of a coordinate transformation for the solution of the Navier-Stokes equations. *J. Comput. Phys.*, **17**, 209–228
- Geleyn, J.-F. 1987 Use of a modified Richardson number for parameterizing the effect of shallow convection. *J. Meteorol. Soc. Jpn*, Special NWP symposium volume, 141–149
- Geleyn, J.-F., Bazile, E., Bougeault, P., Déqué, M., Ivanovici, V., Joly, A., Labbé, L., Piédelièvre, J.-P., Piriou, J.-M. and Royer, J.-F. 1995 'Atmospheric parametrization schemes in Météo-France's ARPEGE N.W.P. model'. Pp. 385–402 in Proceedings of the 1994 ECMWF seminar on physical parametrizations in numerical models, 1995, ECMWF, Reading, UK
- Gregory, D. and Rowntree, P. R. 1991 A mass flux convection scheme with representation of cloud ensemble characteristics and stability-dependent closure. *Mon. Weather Rev.*, **118**, 1483–1506

- Gyakum, J. R., Carrera, M., Zhang, D.-L., Miller, S., Caveen, J., Benoit, R., Black, T., Buzzi, A., Chouinard, C., Fantini, M., Folloni, C., Katzfey, J.-J., Kuo, Y.-H., Lalaurette, F., Low-Nam, S., Mailhot, J., Malguzzi, P., McGregor, J. L., Nakamura, M., Tripoli, G. and Wilson, C. 1996 A regional model intercomparison using a case of explosive oceanic cyclogenesis. *Weather and Forecasting*, **11**, 521–542
- Holtslag, A. A. M. and Boville, B. A. 1993 Local versus nonlocal boundary-layer diffusion in a global model. *J. Climate*, **6**, 1825–1842
- Joly, A., Browning, K. A., Bessemoulin, P., Cammas, J.-P., Caniaux, G., Chalon, J.-P., Clough, S. A., Dirks, R., Emanuel, K. A., Eymard, L., Gall, R., Hewson, T. D., Hilderbrand, P. H., Jorgensen, D., Lalaurette, F., Langland, R. H., Lemaître, Y., Mascart, P., Moore, J. A., Persson, P. O. G., Roux, F., Shapiro, M. A., Snyder, C., Toth, Z. and Wakimoto, R. M. 1999 Overview of the field phase of the Fronts and Atlantic Storm-Track EXperiment (FASTEX) project. *Q. J. R. Meteorol. Soc.*, **125**, 3131–3163
- Kain, J. S. and Fritsch, J. M. 1990 A one-dimensional entraining/detraining plume model and its applications in convective parameterization. *J. Atmos. Sci.*, **47**, 2784–2802
- Källén, E. 1996 'HIRLAM Documentation Manual Level 2–5'. Tech. Report. Swedish Meteorological and Hydrological Institute 1996
- Lopez, P. 2002 Implementation and validation of a new prognostic large-scale cloud and precipitation scheme for climate and data assimilation purposes. *Q. J. R. Meteorol. Soc.*, **128**, 229–257
- Louis, J. F. 1979 A parametric model of vertical eddy fluxes in the atmosphere. *Boundary-Layer Meteorol.*, **17**, 187–202
- Mallet, I., Cammas, J.-P., Mascart, P. and Bechtold, P. 1999 Effects of cloud diabatic heating on the early development of the FASTEX IOP17 cyclone. *Q. J. R. Meteorol. Soc.*, **125**, 3439–3467
- Morcrette, J.-J. 1990 Impact of changes to the radiation transfer parametrizations plus cloud optical properties in the ECMWF model. *Mon. Weather Rev.*, **118**, 847–873
- 1991 Evaluation of model-generated cloudiness: Satellite observed and model-generated diurnal variability of brightness temperature. *Mon. Weather Rev.*, **119**, 1205–1224
- Pinty, J.-P. and Jabouille, P. 1998 'A mixed-phase cloud parameterization for use in a mesoscale non-hydrostatic model: Simulations of a squall line and orographic precipitation'. Pp. 217–220 in Preprints of the AMS conference in cloud physics, 1998, Everett, Washington, USA
- Rasch, P. J. and Kristjánsson, J. E. 1998 A comparison of the CCM3 model climate using diagnosed and predicted condensate parameterizations. *J. Climate*, **11**, 1587–1614
- Redelsperger, J.-L., Brown, P. R. A., Guichard, F., Hoff, C., Kawasima, M., Lang, S., Montmerle, T., Nakamura, K., Saito, K., Seman, C., Tao, W. K. and Donner, L. J. 2000 A GCSS model intercomparison for a tropical squall line observed during TOGA-COARE. Part I: Cloud-resolving models. *Q. J. R. Meteorol. Soc.*, **126**, 823–863
- Roca, R. 2000 'Validation of cloudiness in a GCM using METEOSAT observations'. Proceedings of the ECMWF/EURO-TRMM meeting on the assimilation of rain and clouds into NWP models, 2000, ECMWF, Reading, UK

- Ryan, B. F., Katzfey, J. J.,  
Abbs, D. J., Jakob, C.,  
Lohmann, U., Rockel, B.,  
Rotstain, L. D., Stewart, R. E.,  
Szeto, K. K., Tselioudis, G.  
and Yau, M. K. 2000 Simulations of a cold front by cloud-resolving, limited-area, and  
large-scale models, and a model evaluation using *in situ* and  
satellite observations. *Mon. Weather Rev.*, **128**, 3218–3235
- Savijärvi, H. 1990 Fast radiation parameterization schemes for mesoscale and short-  
range forecast models. *J. Appl. Meteorol.*, **29**, 437–447
- Slingo, A. (Ed.) 1985 *Handbook of the Meteorological Office 11-layer atmospheric  
general circulation model vol. 1: Model description*. DCTN  
29
- 1989 A GCM parametrization for the shortwave radiative properties of  
water clouds. *J. Atmos. Sci.*, **46**, 1419–1427
- Slingo, A. and Wilderspin, R. C. 1986 Development of a revised longwave radiation scheme for an  
atmospheric general circulation model. *Q. J. R. Meteorol.  
Soc.*, **112**, 371–386
- Smith, R. N. B. 1990 A scheme for predicting layer clouds and their water content in a  
general circulation model. *Q. J. R. Meteorol. Soc.*, **116**, 435–  
460
- Stein, J., Richard, E., Lafore, J.-P.,  
Pinty, J.-P., Asencio, N. and  
Cosma, S. 2000 High-resolution non-hydrostatic simulations of flash-flood  
episodes with grid-nesting and ice-phase parametrization.  
*Meteorol. Atmos. Phys.*, **72**, 203–221
- Szeto, K. K. and Guan, H. 2000 Coarse-grid and cloud-resolving simulations of a midlatitude  
cyclonic cloud system: Implications for the parameterization  
of layer clouds in GCMs. *J. Climate*, **13**, 1972–1978
- Wilson, D. R. and Ballard, S. P. 1999 A microphysical based precipitation scheme for the UK Meteorological Office Unified model. *Q. J. R. Meteorol. Soc.*, **125**,  
1607–1636